Title: Membrane curvature governs the distribution of Piezo1 *in cellulo*

Authors: Shilong Yang[1], Steven Arnold[2], Boxuan Li[1], Huan Wang[1], Matthew Wang[3], Charles D. Cox[4], Zheng Shi[1,5]*

[1]Department of Chemistry and Chemical Biology, [2]Department of Cell Biology and Neuroscience, [3]Department of Physics, Rutgers University, Piscataway, New Jersey 08854, United States. [4]Molecular Cardiology and Biophysics Division, Victor Chang Cardiac Research Institute, Sydney, NSW, Australia. [5]Cancer Pharmacology Research Program, Cancer Institute of New Jersey, Rutgers University, New Brunswick, NJ 08901, United States.

** Correspondence should be addressed to: zheng.shi@rutgers.edu*

Abstract:

Piezo1 is a *bona fide* mechanosensitive ion channel ubiquitously expressed in mammalian cells. The distribution of Piezo1 within a cell is essential for various biological processes including cytokinesis, cell migration, and wound healing. However, the underlying principles that guide the subcellular distribution of Piezo1 remain largely unexplored. Here, we demonstrate that membrane curvature serves as a key regulator of the spatial distribution of Piezo1 in the plasma membrane of living cells, leading to depletion of Piezo1 from filopodia. Quantification of the curvature-dependent sorting of Piezo1 directly reveals its nano-geometry *in situ*. Piezo1 density on filopodia increases upon activation, independent of Ca^{2+}, suggesting flattening of the channel upon opening. Consequently, the expression of Piezo1 inhibits filopodia formation, an effect that is abolished with channel activation.

Introduction

Piezo1 is a widely expressed mechanosensitive ion channel in the plasma membrane of eukaryotic cells [1,2], crucial for a broad range of mechanotransduction processes [3-5]. Cryogenic electron microscopy (CryoEM) revealed that Piezo1 contains 38 transmembrane helices and forms a propeller-like trimer which is thought to curve into the cytosol in its resting state [6-9]. Recently, a flattened configuration of Piezo1 was identified when reconstituted into small liposomes, potentially corresponding to the open/inactivated state of the ion channel [10]. The large size and curved architecture of Piezo1 trimers make them directly sensitive to tension in the plasma membrane [11-13]. Additionally, several studies indicate a role for the cytoskeleton in the activation of Piezo channels, while robust evidence for cytoskeletal binding partners remains missing [14-17]. Notably, the cortical cytoskeleton can drastically affect the extent of membrane tension propagation, thereby indirectly controlling Piezo1 activation via the lipid bilayer [18,19].

While the structure and activation of individual Piezo1 channels have been extensively studied, the dynamics and distribution of the channel within a cell are significantly less well explored [20-22]. In addition, it is unclear whether the Piezo1 structures determined *in vitro* recapitulate its nanoscale conformations in live cells [7,10,23]. Interestingly, several recent studies have highlighted a preferential subcellular distribution of Piezo1: First, a polarized distribution of Piezo1 towards the rear of migrating keratinocytes plays a crucial role in controlling the speed of wound healing [24]. Additionally, Piezo1 has been found to enrich in subcellular structures that are important for mechanotransduction, such as focal adhesion sites [20,25] and T-tubules of cardiomyocytes [26]. Lastly, Piezo1 has been reported to preferentially localize to the intercellular bridge during cytokinesis [27]. These intriguing subcellular patterns of Piezo1 raise the question of whether this ion channel can be sorted by fundamental physical factors on the cell surface.

Several hints in the literature indicate that membrane curvature may play a role. First, the structure of purified Piezo1 trimers shows that they form nanoscale invaginations in a simple liposomal system [7]. When locally stretching membrane tethers to activate Piezo1, Ca^{2+} influx was initiated around the tether-cell attachment point where membrane tension was high [18]. However, Ca^{2+} initiation sites were noticeably missing from the highly tensed membrane tether itself. More surprisingly, a recent study showed that force dependent Ca^{2+} signals in filopodia are independent of Piezo channels [28]. Filopodia are highly curved membrane protrusions that geometrically resemble the artificially pulled membrane tethers (tube of radius ~ 50 nm). Thus, a simple explanation would be that Piezo1 are actually absent from these highly curved membrane protrusions.

Here, we show experimentally that membrane curvature is a fundamental regulator of Piezo1's distribution within the plasma membrane. The curvature mismatch between Piezo1 and membrane protrusions prevents the channel from entering structures such as filopodia and thin membrane tethers. Quantifying the curvature preference of Piezo1 on a wide range of tether radii reveals the nano-geometry of Piezo1 *in cellulo*. Furthermore, a chemical activator of Piezo1, Yoda1, which has been hypothesized to serve as a molecular wedge to bias the protein towards a less-curved state [29], allows Piezo1 to enter filopodia in a Ca^{2+}-independent manner. The curvature-preference and Yoda1-response of Piezo1 sorting in cells are consistent with recently determined structural features of purified Piezo1 trimers [10]. The coupling between curvature dependent sorting and activation of Piezo1 in living cells is likely to represent a fundamental cornerstone of Piezo1 channel biology, enabling the regulation of filopodia formation and retaining Piezo1 in the cell body during cell migration.

Results

Piezo1 is depleted from filopodia

To study the distribution of Piezo1 in the plasma membrane, we first co-expressed human Piezo1 (hPiezo1-eGFP[11]) and GPI-anchored mCherry in HeLa cells. Piezo1 traffics well to the plasma membrane, as indicated by an eGFP fluorescence profile across the cell body that closely resembles the co-expressed membrane marker (Fig. 1A). However, the Piezo1 signal was noticeably missing on filopodia that protrudes around the edge of the cell, in drastic contrast with membrane markers such as GPI and CaaX, and with other transmembrane proteins such as the dopamine receptor D2 (D2R) and the mechanosensitive potassium channel TREK1 (Fig. 1A-1C and Fig. S1). To systematically quantify protein densities on filopodia, we defined a unitless filopodia sorting value (S_{filo}) using the fluorescence ratio between the molecule of interest (MOI) and the membrane reference (Fig. S2, Methods). The fluorescence ratio along a filopodium is normalized to the same ratio on a flat region of the cell body to account for cell-cell variabilities. Additionally, the well-defined membrane geometry on a flat region of the cell allows us to directly quantify the diffraction-limited radii of filopodia from the fluorescence of membrane markers[18].

We found the S_{filo} of Piezo1 is close to 0, significantly smaller than the sorting of other MOIs (S_{filo} ~ 1; Fig. 1D). The lack of Piezo1 on filopodia is independent of imaging temperature, the choice of fluorescent protein (FP) tags, FP fusion position, and Piezo1 species (Fig. 1D). Notably, D2R and TREK1 are significantly enriched on filopodia (S_{filo} > 1). The filopodia enrichment of D2R agrees with established membrane curvature preference of GPCRs[30], whereas the enrichment of TREK1 potentially reflects the protein's role in filopodia formation[31].

Cells that overexpress Piezo1 have the same filopodia radii as cells expressing membrane markers, in contrast with the significantly reduced filopodia radii in D2R overexpressing cells (Fig. 1E). Piezo1 was also depleted from the filopodia of HEK293T cells (Fig. S3), however, the non-flat geometry of most HEK293T cells made the quantification of filopodia radii challenging.

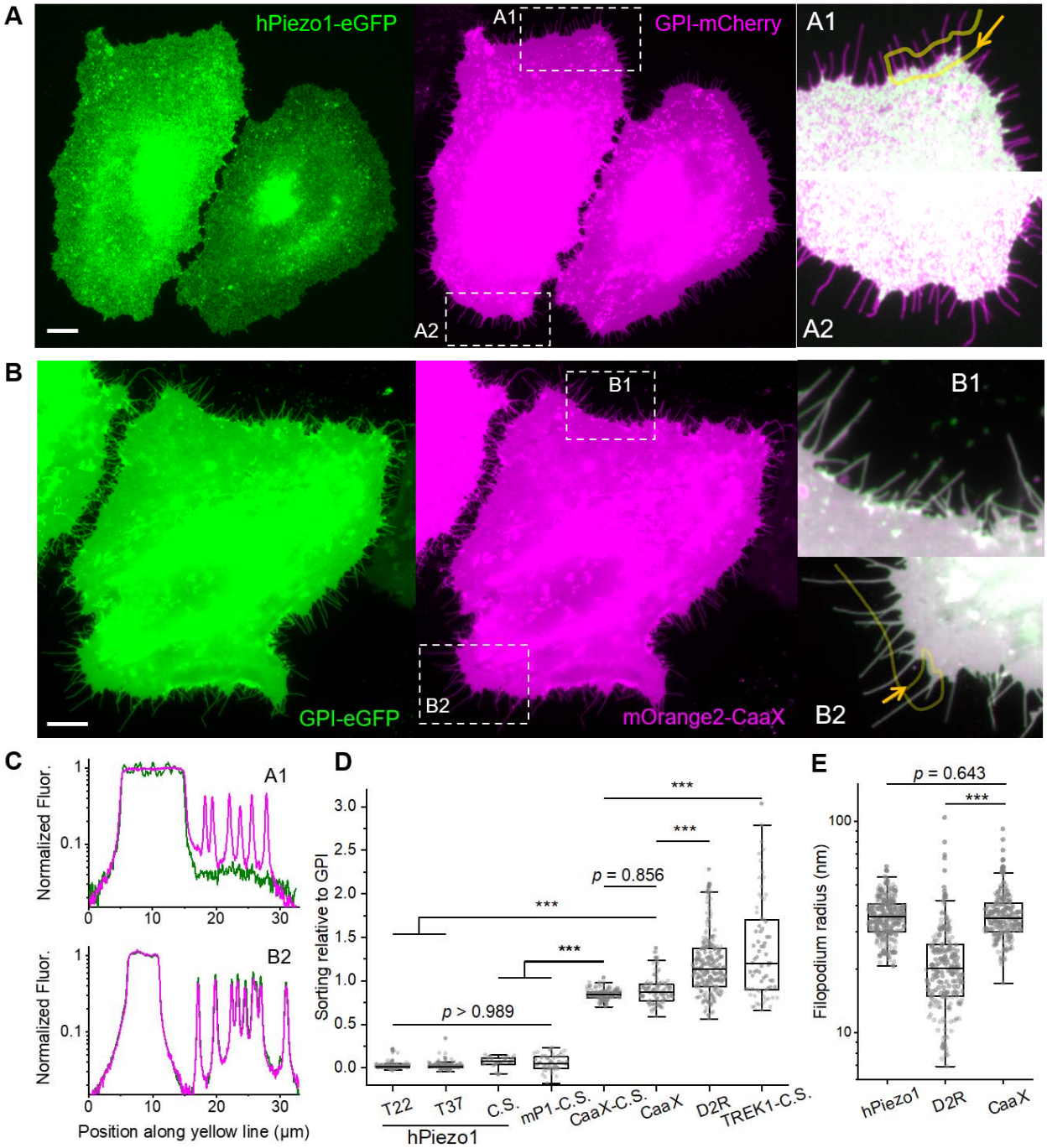

Figure 1. Piezo1 is depleted from filopodia. (A) Fluorescence images of HeLa cells co-expressing hPiezo1-eGFP (green) and GPI-mCherry (magenta). The two boxed regions (A1, A2) are merged and contrast-adjusted on the right. **(B)** Fluorescence images of HeLa cells co-expressing GPI-eGFP (green) and mOrange2-CaaX (magenta). The two boxed regions (B1, B2) are merged and contrast-adjusted on

the right. All scale bars are 10 µm. **(C)** Fluorescence intensity profiles along the marked yellow lines in A1 (up) and B2 (down). Green: hPiezo1 (up) and GPI (down). Magenta: GPI (up) and CaaX (down). **(D)** Filopodia sorting of eGFP fused hPiezo1 (T22: at 22 ^{o}C, n.f. = 129, n.c. = 12; T37: at 37 ^{o}C: n.f. = 113, n.c. = 8), CaaX (n.f. = 87, n.c. = 9), and D2R (n.f. = 222, n.c. = 15) relative to GPI-mCherry. C.S.: color swap, indicating the molecule of interest was fused with mCherry (or mOrange2 for CaaX) while the reference was GPI-eGFP. hPiezo1-C.S.: n.f. = 24, n.c. = 4; mP1-C.S. (mouse Piezo1): n.f. = 47, n.c. = 8; CaaX-C.S.: n.f. = 123, n.c. = 9; TREK1-C.S.: n.f. = 73, n.c. = 12. n.f.: number of filopodia, n.c.: number of cells. **(E)** Filopodia radii of cells co-expressing GPI and hPiezo1 (n = 266), DRD2 (n = 222), or CaaX (n = 210). All radii were determined from the GPI channel. All quantifications were done in HeLa cells except the sorting of TREK-1 was measured in HEK293T cells. *p* values given by one-way ANOVA with *post hoc* Tukey's test. ***$p < 10^{-7}$.

The absence of Piezo1 on filopodia is consistent with the dispensability of Piezo1 for mechanically activated Ca^{2+} signals in filopodia[28]. Additionally, the quantified curvature preference of Piezo1 (S_{filo} = 0.027 ± 0.003, mean ± SEM same below) is in good agreement with a recent observation with CryoEM that only ~3% of purified Piezo1 trimers were oriented 'outside-out', as a Piezo1 trimer on filopodia would be, when reconstituted into highly curved liposomes[10].

<u>Depletion of Piezo1 is not specific to filopodia and is independent of cytoskeleton</u>

Cellular protrusions such as filopodia typically contain a complex network of actin-rich structures [32]. Is the observed depletion of Piezo1 specific to filopodia? To answer this question, we focused our further investigation on membrane tethers that geometrically mimic filopodia but lack specific actin-based structures when freshly pulled (Fig. 2A) [18].

Similar to the observation on filopodia, tethers pulled from HeLa cells co-expressing hPiezo1 and GPI only contained signal for the GPI membrane marker (Fig. 2B), and no significant difference could be found between Piezo1's sorting on tethers (S_{teth}) and on filopodia (S_{filo}) (Fig. 2E). The geometrical similarity between tethers and filopodia (both are highly curved membrane protrusions) points to a possible role of membrane curvature in mediating the sorting of Piezo1. However, S_{filo} didn't show any apparent dependence on filopodium radius, unlike that of D2R (Fig. S4). Additionally, S_{teth} is independent of the relaxation of pulled tethers (Fig. S5). Notably, filopodia only present a small range of membrane radii (25 to 55 nm). Radii of short and fully relaxed tethers are similar to those of filopodia, while stretched tethers are typically thinner (Fig. 2F)[18]. Therefore, we hypothesized that the sorting of Piezo1 maybe most sensitive to low membrane curvatures (radii > 50 nm). Alternatively, it is plausible that Piezo1 is strongly attached to the cortical cytoskeleton, preventing the channel from moving onto membrane protrusions.

To test the two hypotheses, we generated stable membrane blebs via pharmacological depolymerization of the actin cytoskeleton[18]. Similar to previous reports, Piezo1 clearly locates to bleb membranes (Fig. 2C, 2D)[11]. More importantly, negligible Piezo1 fluorescence was observed on membrane tethers pulled from tense blebs (Fig. 2C). Plasma membrane blebs do not contain any cytoskeleton, therefore results such as Fig. 2C directly argue against a main cytoskeletal role in the depletion of Piezo1 from tethers. The radius of a tether pulled from the bleb is determined by the bleb's membrane tension[18], which is in turn governed by the intracellular pressure[33]. We found that membrane blebs triggered by actin depolymerization exhibited a wide range of apparent 'floppiness', likely a result of stochastic pressure release during bleb formation. On floppy (i.e., low membrane tension) blebs, pulled tethers showed

much wider apparent radii (Fig. 2D). Importantly, Piezo1 fluorescence can be clearly observed on these wide tethers, leading to a highly scattered S_{teth} of Piezo1 on tethers pulled from blebs (Fig. 2E).

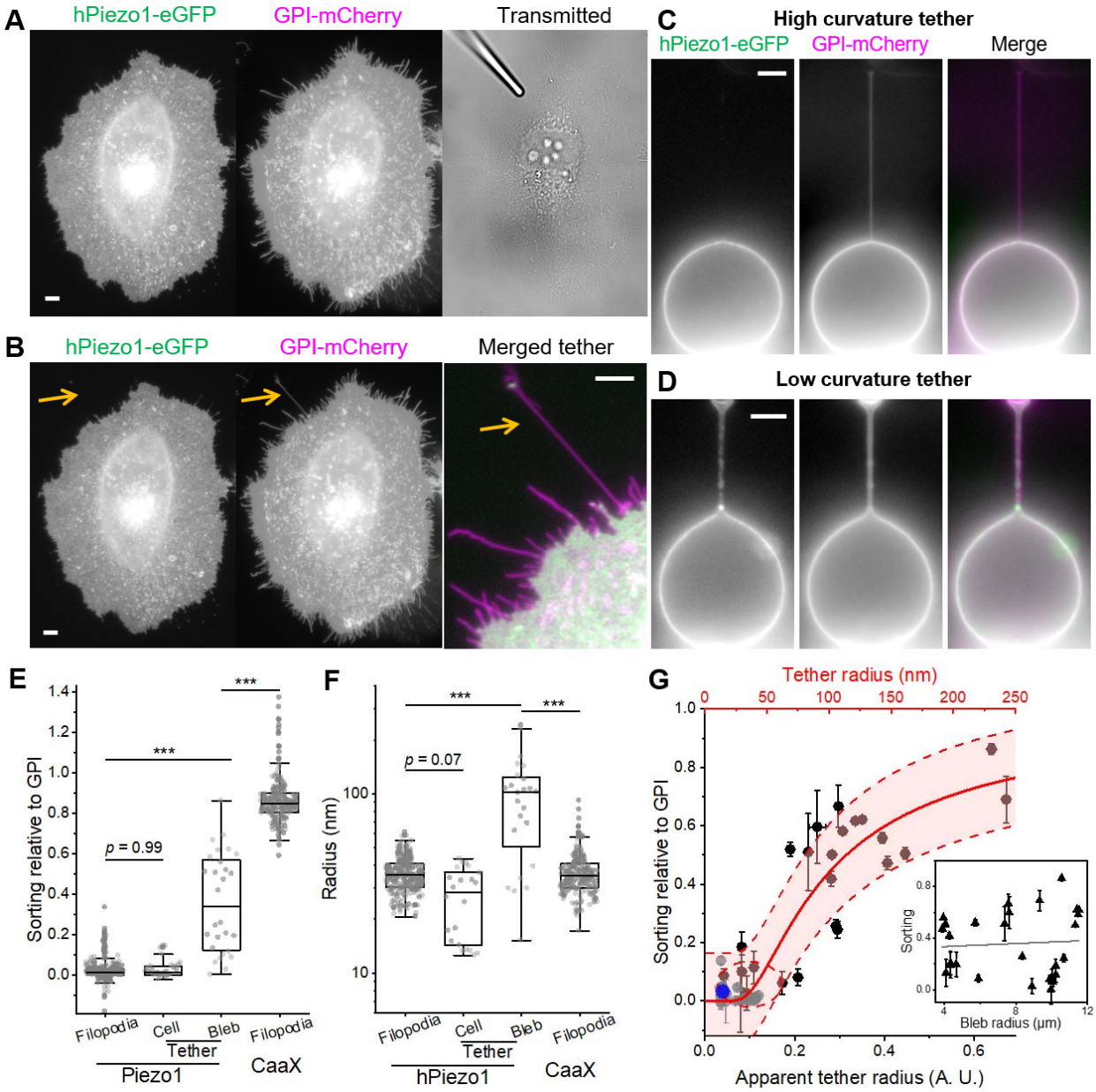

Figure 2. Sorting of Piezo1 on membrane tethers. (A) Fluorescence images of a HeLa cell co-expressing hPiezo1-eGFP (left) and GPI-mCherry (middle). The transmitted light image (right) shows the position of a motorized micropipette (fused) in contact with the cell before tether pulling. **(B)** Fluorescence images of the HeLa cell in (**A**) after a 20 µm tether was pulled out (arrow). The tether region is merged and contrast-adjusted on the right. **(C, D)** Fluorescence images of tethers pulled from membrane blebs on HeLa cells co-expressing hPiezo1-eGFP (left) and GPI-mCherry (middle). Merged images shown on the right. Significantly less Piezo1 signals were observed on the tether from tense bleb (**C**) compared to the tether from floppy bleb (**D**). All fluorescence images here are shown in log-scale to highlight the dim tether. All scale bars are 5 µm. **(E)** Sorting of Piezo1 on tethers pulled from cell membranes (Cell, n = 31) and membrane blebs (Bleb, n = 28) relative to GPI. Filopodia sorting of Piezo1 (n = 313) and CaaX (n =

210) from Fig. 1D are shown here for comparison. (**F**) Radii of tethers pulled from cell membranes (Cell) and membrane blebs (Bleb, converted to absolute tether radii) co-expressing GPI and hPiezo1. Radii of filopodia on cells co-expressing GPI and hPiezo1 or CaaX (Fig. 1E) are shown here for comparison. All radii were determined from the GPI channel. (**G**) Sorting of hPiezo1 on tethers pulled from blebs (black) plotted as a function of the apparent (lower axis) and absolute (upper axis) radii of the tethers. Sorting of hPiezo1 on tethers pulled from cells are shown in gray. The fraction of 'outside-out' Piezo1 when reconstituted into small liposomes (according to ref[10]) is shown in blue. The red circle shows the cluster of tense bleb data used to calculate the conversion factor for tether radius (361 ± 61 nm/A.U.). The radius of the thickest tether was converted to 242 nm, consistent with the directly measured upper limit of tether radii (264 nm; Fig. S6). The solid line is a two-parameter fit (R^2 = 0.85) with the shaded area representing the 95% confidence interval. Insect: Sorting of Piezo1 as a function of bleb radius, where the line represents a linear fit with slope = 0.005 ± 0.017 μm^{-1}. Error bars are SEM. *p* values given by one-way ANOVA with *post hoc* Tukey's test. ***$p < 10^{-7}$.

When combining the Piezo1 sorting and tether radius measurements together, a clear positive correlation can be observed, with S_{teth} on tense blebs comparable to S_{teth} measured on intact cells and to the fraction of 'outside-out' Piezo1 trimers when reconstituted into small liposomes (Fig. 2G)[10]. S_{teth} of Piezo1 is independent of bleb radius (Fig. 2G, insect), confirming the lack of optical artifacts induced by bleb curvature. However, the curved geometry of blebs only allowed determination of an apparent tether radius (Fig. S2). We assumed that the average radius of filopodia and equilibrated tethers from cell body are equal to the radii of tethers from tense blebs, thus converting the apparent radii (in A.U.) to absolute radii (in nm) of tethers from blebs (Fig. 2F, 2G). The conversion was consistent with the upper bound of tether diameters set by the width of optically resolvable catenoid-shape membranes at the two ends of low-tension tethers (Fig. S6).

Quantification of Piezo1's molecular features

The trimer of Piezo1 has been suggested to adopt a dome shape (~10 nm radius) in liposomal systems[7,10]. If this were to occur *in cellulo*, Piezo1 would energetically prefer negatively curved membrane invaginations and stay away from positively curved membrane protrusions such as the filopodium and tether. Accordingly, we fitted our measured relation between the sorting of Piezo1 on tether (S_{teth}) and the tether radius (R_t) to a 2-parameter model based on the bending energy of the membrane (Fig. 2G, Methods)[30,34]:

$$S_{teth} = \exp\left[-\widetilde{A_P}\left(\frac{1}{{R_t}^2} - \frac{2C_0}{R_t}\right)\right] \quad (1)$$

Where $\widetilde{A_P} = \frac{\tilde{\kappa} A_P}{2k_B T}$ is the product of individual Piezo1 unit area (A_p) and the bending stiffness of the protein-membrane complex ($\tilde{\kappa}$), normalized by the Boltzmann constant (k_B) and the absolute temperature (T). C_0 is the spontaneous curvature of each protein-membrane complex and is expected to be negative for Piezo1.

The two fitting parameters $\widetilde{A_P}$ and C_0 correspond to the contributions of Piezo1's size (larger proteins have a stronger tendency to stay away from highly curved membranes) and intrinsic curvature, respectively. The fitting gave $\widetilde{A_P}$ = 2500 ± 1200 nm^2 and $-C_0^{-1}$ = 87 ± 21 nm. Combining tether pulling force and tether radius measurements[18], we determined the membrane bending stiffness of the Piezo1 expressing cells to be 13.6 ± 3.8 k_BT (Fig. S7, n = 9), giving an estimated area of the protein A_P = 370 ± 180 nm^2, in agreement with the area of Piezo1 trimers measured with CryoEM (~400 nm^2)[10,13,23]. The spontaneous curvature of the Piezo1-membrane

complex C_0 represents a balance between the preferred curvature of Piezo1 trimers (-0.2 nm^{-1}, corresponds to 10 nm spherical invaginations as suggested by CryoEM studies[10]) and that of the associated membrane (C_0 = 0 nm^{-1}), consistent with the large amount of lipids associated with the dome of the propeller-shaped Piezo1 trimers[7,10].

Our data and model, which do not assume to know any molecular detail of Piezo1 and is limited by optical resolution (~500 nm), reveal nano-geometry of the channel on the order of 10 nm and are in surprising agreement with the CryoEM results of purified Piezo1 trimers[7,8,10,23]. The model assumes that Piezo1 behaves as 2-dimentional ideal gas in the membrane. While the assumption is consistent with the observation that Piezo1 trimers function independently[35], we did neglect potentially important intermolecular interactions between Piezo1 trimers[21,36,37].

Although our measurements are focused on membrane protrusions (positive R_t), the model (equation 1) can be directly extended to study Piezo1 on membrane invaginations (negative R_t). It is worth noting that contributions from the size and the spontaneous curvature of Piezo1 are synergistic in the case of protrusions but cancel each other out on invaginations. Therefore, the enrichment of Piezo1 onto invaginations is predicted to be much less prominent than the depletion of Piezo1 from protrusions, with S_{teth} peaks at 1.39 when R_t = -87 nm (Fig. S8, Methods). The average enrichment of Piezo1 is predicted to be only 2% on 25 ~ 75 nm invaginations compared to an 87% depletion effect on protrusions of the same curvature range. This is consistent with the lack of obvious Piezo1 enrichment spots in the bulk of plasma membrane where highly curved invaginations such as endocytic sites and caveolae are expected (Fig. 1A, 2A, 2B, S1-S5). Future studies with higher resolution and better-defined invagination curvature (such as nanopatterned surfaces [38]) will be required to clarify the detailed sorting behavior of Piezo1 on membrane invaginations.

<u>Yoda1 leads to a Ca^{2+} independent increase of Piezo1 on tethers</u>

Yoda1 is a Piezo1 agonist that has been hypothesized to bias the protein towards a less-curved state[29]. Equation (1) predicts that a smaller $|C_0|$ would lead to an increase of Piezo1 density on protrusions. Indeed, a significantly increased amount of Piezo1 signal was observed after adding 10 μM of Yoda1, while the radii of these filopodia remain unaltered (Fig. 3A-C, S9A). Additionally, the S_{filo} of activated Piezo1 showed a positive correlation with filopodia radii (Fig. 3D; Pearson's r = 0.61). Assuming the size of Piezo1 doesn't change during activation ($\widetilde{A_P}$ = 2500 nm^2), our model predicts an intrinsic curvature $-C_0^{-1}$= (5 ± 60) μm of Piezo1 in the presence of Yoda1, corresponding to an essentially flat geometry (Fig. 3D, S8). The Yoda1 effect on Piezo1 sorting was not instantaneous, taking more than 5 min to equilibrate (Fig. S10A). This is consistent with the measured mean diffusion coefficient of Piezo1 on the cell membrane (Fig. S10B; 0.0021± 0.0004 $\mu m^2/s$, n = 44), indicating that Piezo1 trimers diffuse from the cell body to filopodia after Yoda1-induced activation.

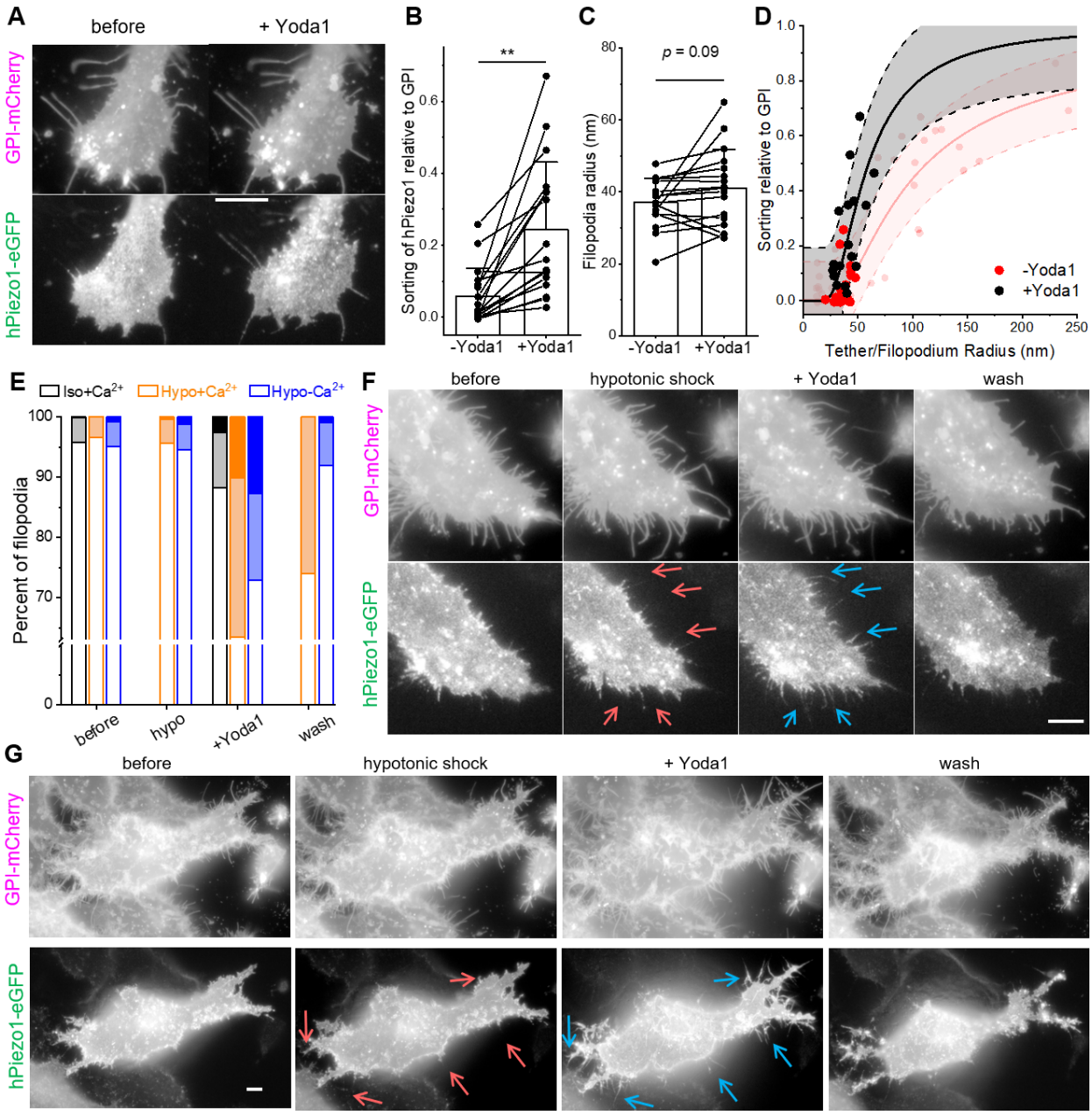
A
before
+ Yoda1
GPI-mCherry
hPiezo1-eGFP
B
Sorting of hPiezo1 relative to GPI
**
-Yoda1
+Yoda1
C
Filopodia radius (nm)
p = 0.09
-Yoda1
+Yoda1
D
Sorting relative to GPI
Tether/Filopodium Radius (nm)
-Yoda1
+Yoda1
E
Iso+Ca2+
Hypo+Ca2+
Hypo-Ca2+
Percent of filopodia
before
hypo
+Yoda1
wash
F
before
hypotonic shock
+ Yoda1
wash
GPI-mCherry
hPiezo1-eGFP
G
before
hypotonic shock
+ Yoda1
wash
GPI-mCherry
hPiezo1-eGFP

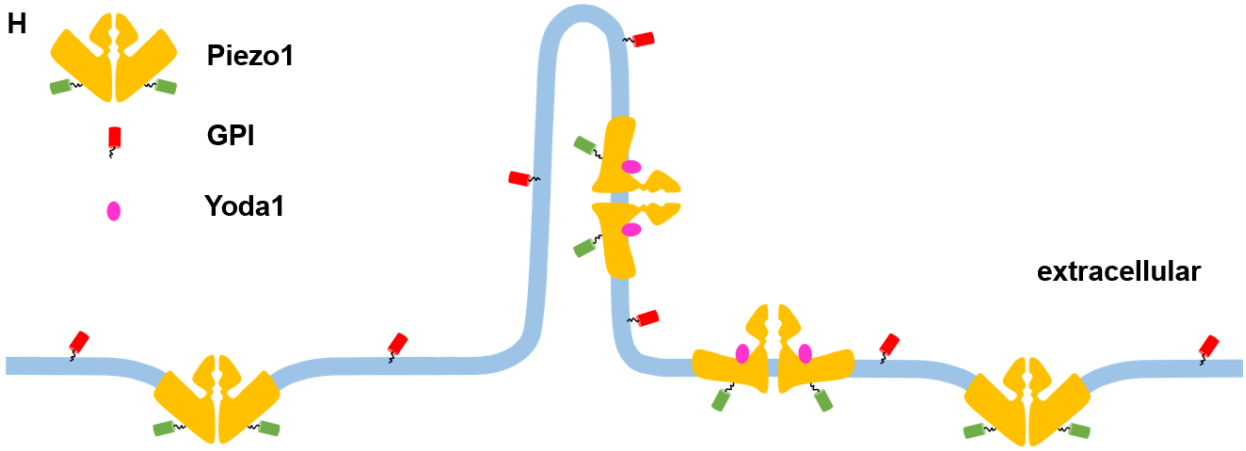
H
Piezo1
GPI
Yoda1
extracellular

Figure 3. Activation via Yoda1 leads to increased sorting of Piezo1 on filopodia, independent of Ca^{2+}. (A) Left: fluorescence images of a HeLa cell (see Fig. S9A for the full cell) co-expressing GPI-mCherry (up) and hPiezo1-eGFP (down). Right: 10 min after adding 10 µM Yoda1 to the cell on the left. **(B, C)** Quantifications of hPiezo1 sorting on filopodia (**B**) and filopodia radii (**C**) for the cell in **A**. *p* values given by paired Student's t test, $^{**}p < 10^{-3}$. **(D)** S_{filo} plotted as a function of filopodia radius before (red) and after (black) adding Yoda1. The black line is a one-parameter fit of the +Yoda1 data to equation (1) with $\widetilde{A_P}$ fixed at 2500 nm^2. Shaded area represents the 95% confidence interval. Fitted $-C_0^{-1}$ = (5 ± 60) µm. Data from Fig. 2G are shown in light red for comparison. **(E)** Percentage of filopodia that showed strong (S_{filo} > 0.3, dark), medium (0.1 < S_{filo} < 0.3, light), and weak (S_{filo} < 0.1, open) sorting of hPiezo1 under the labelled conditions. Black: no osmotic shock, regular XC (n = 752); Orange: hypotonic shock, regular XC (n = 564); blue: hypotonic shock, Ca^{2+}-free XC (n = 771). **(F-G)** Fluorescence images of HeLa cells in regular (**F,** see Fig. S9B for the full cell) and Ca^{2+}-free (**G**) XC buffer. Up: GPI-mCherry. Down: hPiezo1-eGFP. Left to right: before treatments; 10 min after swelling with regular (**F**) or Ca^{2+} free (**G**) hypotonic buffer; 20 min after adding 10 µM Yoda1 (dissolved in regular (**F**) or Ca^{2+} free (**G**) hypotonic buffer); after washing 3 times with regular (**F**) or Ca^{2+} free (**G**) XC buffer. Red/blue arrows point to the filopodia where Piezo1 signals were absent/enhanced before/after adding Yoda1. All fluorescence images here are shown in log-scale to highlight the filopodia. All scale bars are 5 µm. **(H)** Illustration showing the membrane curvature sorting of Piezo1 and the effect of Yoda1 on the curvature sorting of Piezo1.

Under regular cell culture conditions, we noticed that only a small portion of filopodia (~10%) showed measurably changed Piezo1 signal in response to the Yoda1 treatment (Fig. 3E). We reasoned that the opening of Piezo1 resembles a sharp two-state transition[13], and the main effect of Yoda1 is to lower the transition tension[29]. Piezo1 cannot be opened by Yoda1 if the resting tension of the cell is too low, whereas channels that are in a pre-stressed (yet closed) state would have higher chance to respond to Yoda1. To test this, we pre-stressed the cells with hypotonic shock. The hypotonic shock itself didn't significantly change the sorting of Piezo1 on filopodia. However, significantly more (~35%) filopodia responded to a subsequent Yoda1 treatment (Fig. 3E, 3F, S9B, S10C). Importantly, Yoda1-induced S_{filo} of Piezo1 is not a result of Ca^{2+} influx, as a similar effect can be observed on cells maintained in a Ca^{2+}-free buffer (Fig. 3E, 3G). Finally, Yoda1 induced sorting of Piezo1 is reversible as Piezo1 signals disappear from filopodia after washing out Yoda1 (Fig. 3E-G). The flattening of Piezo1 during activation has been suggested *in silico*[36,39] and recently partially confirmed via *in vitro* reconstitutions[10]. Our study shows this conformational change of Piezo1 in live cells (Fig. 3H).

Piezo1 inhibits filopodia formation

Curvature sensing proteins often have a modulating effect on membrane geometry: I-BAR proteins that sense positive curvature can generate more protrusions [32], whereas N-BAR proteins that sense negative curvature help induce membrane invaginations such as endocytic vesicles (note that the sign of curvature is defined oppositely compared to some of the literature [40]). Thus, we hypothesize that Piezo1 can have an inhibition effect on the formation of filopodia.

Indeed, HeLa cells with higher expression level of hPiezo1-eGFP tend to have less filopodia (Fig. 4A, 4B). However, due to the overall low expression of hPiezo1-eGFP in the majority of HeLa cells, only a weak negative correlation was observed between filopodia number and hPiezo1-eGFP fluorescence in each cell (Fig. 4B). In HEK293T cells where hPiezo1-eGFP expresses 3.5-fold higher, a stronger negative correlation was observed between the number of filopodia per cell and hPiezo1-eGFP density on the cell membrane (Fig. 4C, 4D). Interestingly, the negative correlation was almost completely abolished when HEK293T cells were cultured in 5 µM Yoda1 (Fig. 4C), consistent with Yoda1's ability to reduce the curvature effects of Piezo1 (Fig. 3H).

The antagonistic effect of Piezo1 on the formation of filopodia is consistent with several recent observations: First, knocking out Piezo in Drosophila promotes axon regeneration[41]. Secondly, Piezo1 negatively regulates the morphological activity (i.e., number of protrusions) of muscle stem cells[42]. Lastly, Piezo2 inhibits neurite outgrowth in N2a cells[16]. In addition to membrane curvature, specific Piezo regions and Ca^{2+} signaling induced by the activation of Piezo can also play important roles in regulating filopodia formation and growth[16,41,42]. Further studies are required to fully dissect the contribution of each of these variables.

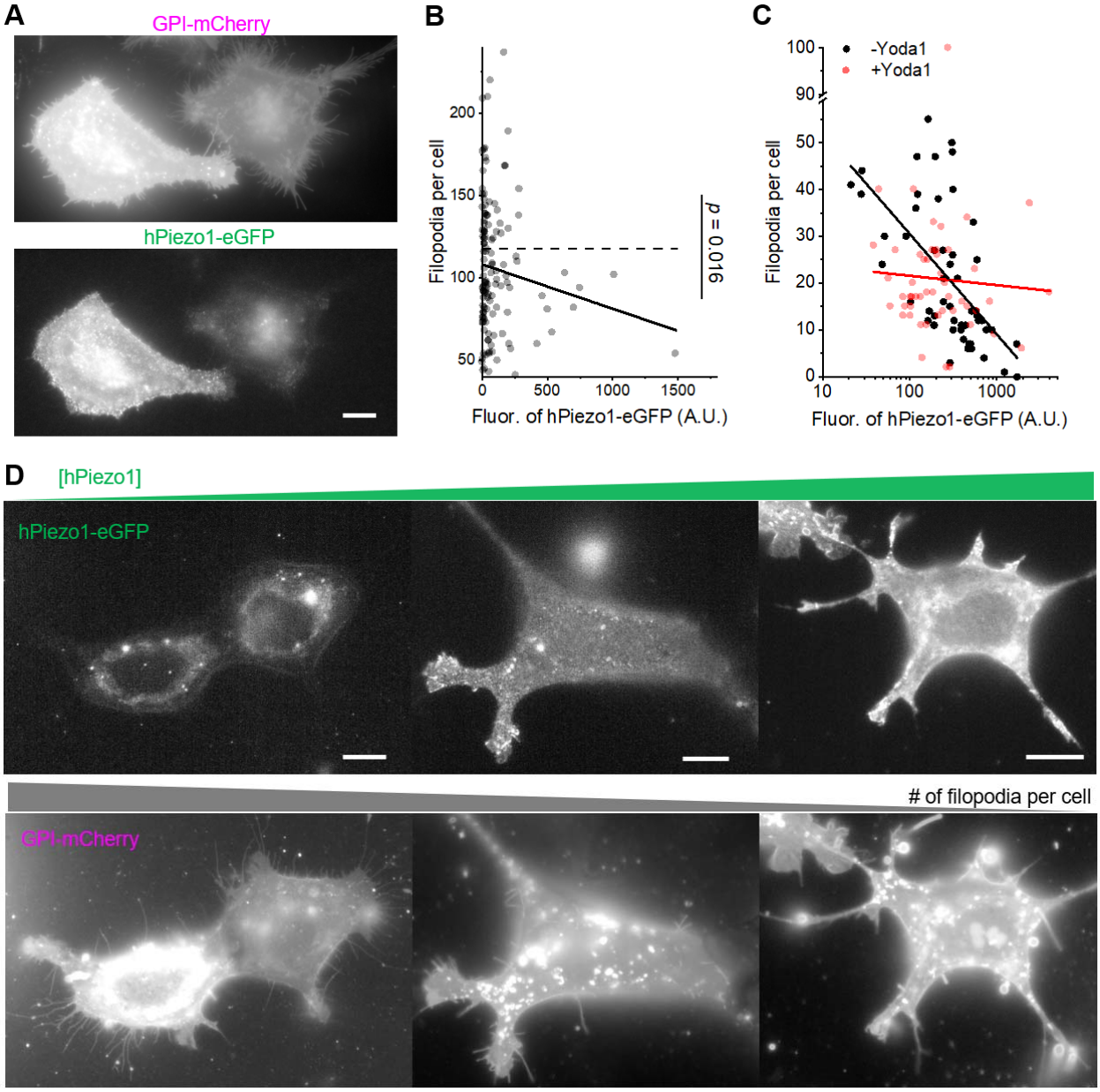

Figure 4. Piezo1 inhibits filopodia formation. (A) Fluorescence images of HeLa cells co-expressing GPI-mCherry (up) and hPiezo1-eGFP (down). **(B)** Relation between the number of filopodia and hPiezo1-eGFP expression level in HeLa cells (n = 129). Dash line represents the average number (118) of

filopodia per cell. Solid line represents a linear fit (Pearson's r = -0.13). *p* value given by Student's t test. **(C)** Relation between the number of filopodia and hPiezo1-eGFP expression level in HEK293T cells cultured in regular (black, n = 52) and 5 µM Yoda1 containing (red, n = 50) media. Lines are linear fits between y and log(x). Without Yoda1 (black): slope = -21.5 ± 4.0, Pearson's r = -0.61. With Yoda1 (red): slope = -2.0 ± 5.0, Pearson's r = -0.06. **(D)** Fluorescence images of HEK293T cell co-expressing GPI-mCherry (up) and hPiezo1-eGFP (down). Cells are arranged so that the expression level of hPiezo1-eGFP increases from left to right, the number of filopodia per cell decreases correspondingly. All fluorescence images here are shown in log-scale to highlight the filopodia. All scale bars are 10 µm.

Discussion

The curved structure of Piezo1 trimers has been suggested to play an important role in the activation of the channel[7,10,13,23]. Our study demonstrates that the coupling of Piezo1 to nanoscale membrane curvature also regulates the distribution of Piezo1 within the plasma membrane. Our quantifications in live cells are in good agreement with CryoEM studies of purified Piezo1[7,10,23]. Our experiments also strongly support the long-hypothesized flattening of Piezo1 during activation[7,10,29], thereby coupling the activation of the channel to its subcellular distribution.

Membrane curvature sensing has been studied for a range of proteins including BAR domain proteins and GPCRs[30,34,40], our report represents the first such study for a mechanosensitive ion channel. Additionally, the large area of Piezo1 (more than 10-fold larger than a typical GPCR) gives rise to a prominent protein-size effect that has often been neglected when studying smaller membrane proteins (Fig. S8)[30,40]. In addition to membrane curvature, tension in the membrane may also play a role in regulating the subcellular distribution of the protein[22]. Membrane tension is homogeneous (equilibrates within 1 s) within free membranes such as the blebs and tethers[18]. Our measurements on tethers pulled from blebs (Fig. 2C-G) therefore shows that membrane curvature can directly modulate Piezo1 distribution beyond potential confounding tension effects.

In addition to regulating the formation of filopodia (Fig. 4), the curvature sensing of Piezo1 can have a direct benefit of making sure that the protein is retained at the rear edge during cell migration and avoid losing Piezo1 to retraction fibers (e.g., Fig. S3B)[24]. Moreover, the dynamics of filopodia is often linked to the metastatic transition of cancer cells[32], suggesting new roles of Piezo1 in cancer biology[25].

Overall, our study suggests that the curvature sensing of Piezo1 provides nanoscale input for the channel in live cells and is a universal regulator of the channel's distribution within cell membranes. These features are likely to be of fundamental importance to a wide range of Piezo1-dependent biological processes.

Methods

<u>Cell culture, transfection, bleb formation, osmotic shock, and Yoda1 treatment</u>

HeLa cells (ATCC and from Renping Zhou lab) were cultured in Eagle's Minimum Essential Medium (EMEM) supplemented with 10% Fetal Bovine Serum (FBS) and 1% Penicillin/Streptomycin (PS). HEK293T cells (from Zhiping Pang lab) were cultured in Dulbecco's Modified Eagle Medium (DMEM) supplemented with 10% FBS, 1% PS and 1%

Sodium Pyruvate. Both cell lines were seeded in 100 mm plastic dishes with ~ 1×10^6 cells per dish. Cells were kept in incubator with 5% CO_2 and 100% relative humidity at 37°C.

For fluorescence imaging, cells were transfected in 35 mm plastic dishes at around 60% confluency. For HeLa cells, a mixture of 125 µL Opti-MEM, 3.5 µL TransIT-X2 and 300 ng of each plasmid DNA were added after 12 min incubation. For HEK293T cells, a mixture of 250 µL Opti-MEM, 5 µL P3000 reagent, 3.5 µL Lipofectamine reagent and 500 ng of each plasmid DNA were added after 15 min incubation. Cells were kept in incubator for 24 hours before further split onto 35 mm precoated (Poly-D-Lysine for HeLa cell and Matrigel for HEK293T cell) glass bottom dishes (Cellvis) for imaging. Cells were imaged 12-48 hours after splitting.

Before imaging, cell culture medium was replaced with extracellular imaging buffer (XC buffer) containing 125 mM NaCl, 2.5 mM KCl, 15 mM HEPES, 30 mM Glucose, 1 mM $MgCl_2$ and 3 mM $CaCl_2$ with pH 7.3. Ca^{2+} free experiments were done by omitting $CaCl_2$ in the XC buffer. Hypotonic osmotic shock was carried out by using a diluted XC buffer that is 0.25 ~ 0.5 of its initial concentration.

To trigger blebs, HeLa cells were incubated with 400 µL of 100 ~ 200 µM Latrunculin B (diluted in XC buffer) for 5 min. Additional XC buffer was added after bleb formation to keep a final Latrunculin concertation of 20 ~ 40 µM during experiments.

For experiments in Fig. 4, stock solution of Yoda1 (5 mM, dissolved in DMSO) was diluted to 5 µM in EMEM before use. Cells were incubated with 5 µM Yoda1 solution for 2 to 4 hours. Control group was incubated with 0.1% DMSO for same amount of time. After incubation, culture media were carefully replaced with XC buffer containing the same concentrations of Yoda1 or DMSO. For experiments in Fig. 3, stock solution of Yoda1 was diluted to 10 µM in XC buffer before use. The number of filopodia per cell in Fig. 4 was counted manually for all protrusions that are longer than 1 µm, counting was independently verified by two researchers and by FiloDetect [43].

Imaging, tether pulling, and quantification

Fluorescence imaging was done on either a Leica DMi8 or a Nikon Ti2-A inverted microscope. Leica DMi8 was equipped with an oil-immersion objective (100X; NA 1.47; Leica) and laser excitation (488 nm for eGFP and 561 nm for mCherry or mOrange2). Nikon Ti2-A microscope was equipped with LED excitation (~470nm for eGFP and ~550 nm for mCherry or mOrange2) and either a water-immersion objective (60X; NA 1.20; Nikon) or an oil-immersion objective (100X; NA 1.30; Nikon). The oil objective was integrated with an objective heater (OKO lab) for 37 ^{o}C measurements. Temperature was calibrated by directly measuring the temperature of the medium near the imaged cell. The Leica DMi8 was integrated with an Infinity Scanner (Leica) for fluorescent recovery after photobleaching (FRAP) experiments. The Nikon Ti2-A microscope was integrated with micromanipulators (PatchPro-5000, Scientifica) and an optical tweezer (Tweez305, Aresis) for tether pulling and force measurements. Images were analyzed with ImageJ and Matlab (R2019a).

Membrane tethers were pulled from HeLa cells or cell-attached membrane blebs using either a motorized micropipette[44] with a fused tip or a polystyrene bead (4.5 µm) trapped with an optical tweezer.

Membrane curvature sorting and filopodia/tether radii were calculated according to the illustration in Fig. S2. We hypothesize that filopodia and membrane tether are cylindrical membrane tubes, and that the quantum yields of fluorescent proteins are independent of local curvature. For radius calculation, we also assume that both bilayers of a flat region of the cell are captured in widefield epi-fluorescence images [18].

For membrane tube with a diffraction-limited radius *r*, if a region of interest (ROI) is drawn to cover a length *L* of the tube (Fig. S2B), the total membrane area with the ROI is given by

$$A_{tube} = 2\pi r L \quad (\mathrm{eq.\,S1})$$

Assume I_{mean}^{tube} is the background-corrected mean fluorescence within the ROI on the tube, A_{ROI} is the area of the ROI, the total fluorescence should equal to the number density of FPs on membrane (*ρ*) multiplied by A_{tube} and by the fluorescence per FP (*β*).

$$I_{mean}^{tube} \cdot A_{ROI} = A_{tube} \cdot \rho \cdot \beta \quad (\mathrm{eq.\,S2})$$

The background-corrected mean fluorescence within the ROI on a flat region of the cell membrane (Fig. S2B), I_{mean}^{cell}, is related to *ρ and β by*

$$I_{mean}^{cell} = 2 \cdot \rho \cdot \beta \quad (\mathrm{eq.\,S3})$$

The factor of 2 takes into account the two membrane surfaces of the cell (Fig. S2D).

Combining equations S1 to S3, the radius of the membrane tube is given by

$$r = \frac{I_{mean}^{tube} \cdot A_{ROI}}{\pi L \cdot I_{mean}^{cell}} \quad (\mathrm{eq.\,S4})$$

In principle, *r* can be calculated using the fluorescence of any membrane proteins/lipids, however, only molecules in the membrane that do not have membrane curvature sensitivity can give the real tube radius. When a tether is pulled from a bleb (Fig. 2C and 2D), an apparent radius of the tether was calculated using the background-corrected mean fluorescence within the ROI of the bleb membrane instead of I_{mean}^{cell} (Fig. S2C).

The reported tether and filopodia radii in our study were determined using the fluorescence of GPI-FP. GPI anchors the FP to the outer leaflet of the plasma membrane, due to the relatively large size of FP to the GPI anchor, GPI-FPs may have enrichment towards highly curved protrusions [45]. For the same reason, CaaX-FP, which is anchored to the inner leaflet of the plasma membrane may deplete from membrane protrusions. However, we expect this effect to be less than 7%, as the relative sorting of CaaX to GPI was measured to be 0.863 ± 0.008 (Fig. 1D).

Membrane curvature sorting *S* is the effective number density of a molecule of interest (MOI) on the membrane tube relative to either a flat region on the cell body (Fig. S2B) or the membrane bleb (Fig. S2C).

$$S = \frac{r(MOI)}{r(GPI)} \quad (\mathrm{eq.\,S5})$$

S = 0 when the MOI is completely depleted from the tube. *S* = 1 when the MOI has the same curvature preference as GPI-FP reference.

An ROI width of 0.5 μm was used for all tether/filopodium quantifications. Filopodia that are sufficiently away (> 1 μm) from other membrane structures and more than 3 μm in length were picked for calculating *S* and *r*. Errors in *S* and *r* were propagated using the standard deviation in the background fluorescence as the error for mean fluorescent intensities. In Fig. 3E, filopodia with clear Piezo1 signal on less than 10% of the total length (typically corresponding to $S < 0.1$) were considered as no response; between 10% to 50% of the filopodia (typically corresponding to $0.1 < S < 0.3$) were considered weak response; more than 50% of the filopodia ($S > 0.3$) were considered strong response.

Tether force measurement

To measure tether force, a membrane tether is pulled by a bead trapped with an optical tweezer (Tweez305, Aresis, Slovenia) equipped on the Ti2-A inverted microscope (Nikon, Japan). Membrane tubes were pulled to around 15 μm in length and then held until an apparent equilibrium force *f* was reached (Fig. S7). Then fluorescence images of the cell and the tether were taken for tether radius (*r*) measurements according to eq. S4. Force on the bead was calculated from the displacement of the bead from the center of the trap and the trap stiffness (calibrated before each experiment by applying equipartition theorem to the thermal fluctuation of a trapped bead). Then membrane tension σ and bending stiffness κ_m were be calculated by: [46]

$$\sigma = \frac{f}{2\pi r} \quad (\text{eq. S6})$$

$$\kappa_m = \frac{fr}{2\pi} \quad (\text{eq. S7})$$

Note that the pulling force *f* may contain contributions from the cytoskeleton and membrane asymmetry. Therefore, a more accurate measure of κ_m is to fit $f/2\pi$ vs. r^{-1} to a linear relation where the slope will report κ_m and the intercept will report the aforementioned additional contributions to tether pulling force (Fig. S7).

FRAP measurements

3 to 6 circular ROIs with radius R_{bleach} = 1.5 μm were picked on flat regions of HeLa cell expressing hPiezo1-eGFP. 488nm laser at full power was used to photo bleach the selected ROI for ~ 1 s. Frames before photobleaching and the first frame after photobleaching were used to normalize the fluorescence intensity, background photobleaching was corrected by the fluorescence of the entire cell. The normalized recovery curve *I*(t) was fitted to the following relation to extract half-recovery time ($\tau_{0.5}$, 2-parameter fit):

$$I(t) = \frac{I_0 + \frac{t}{\tau_{0.5}}}{1 + \frac{t}{\tau_{0.5}}} \quad (\text{eq. S8})$$

The diffusion coefficient was calculated by [18,47]:

$$D_s^{cell} = 0.224 \frac{{R_{bleach}}^2}{\tau_{0.5}} \quad (\text{eq. S9})$$

Model for the curvature sorting of Piezo1

We assume the protein-membrane complex has a preferred curvature C_0. In the case of Piezo1, each protein unit would correspond to a trimer of Piezo1 with associated membranes that were deformed, C_0 represents a balanced shape between the curvature preference of the Piezo1 trimmer and the preferred shape of the associated membrane. If we define protrusions (e.g., tethers, filopodia) on the cell to have a positive curvature, then C_0 would be negative for Piezo1 trimers, assuming the associated membrane prefer to be flat.

The energy of putting one unit of protein-membrane complex into a membrane of curvature K:

$$E^{\mathrm{b}} = \frac{1}{2}\tilde{\kappa}A_P(K - C_0)^2 \quad (\mathrm{eq.\,S10})$$

For a flat membrane, K = 0; for filopodia/tether, $K = 1/R_t$. A_p is the area of the protein-membrane complex. $\tilde{\kappa}$ is the bending stiffness of the protein-membrane complex, which is the effective stiffness when bending the membrane (κ_m) and the protein (κ_p) in series:

$$\frac{1}{\tilde{\kappa}} = \frac{1-\theta_p}{\kappa_m} + \frac{\theta_p}{\kappa_p} = \frac{1}{\kappa_m} + \theta_p\left(\frac{1}{\kappa_p} - \frac{1}{\kappa_m}\right) \quad (\mathrm{eq.\,S11})$$

Here, θ_p is the area fraction of the protein in each unit of the protein-membrane complex. Measurements of the overall membrane bending stiffness of Piezo1 expressing cells ($\sim\kappa_m$), therefore serve as a good estimation for $\tilde{\kappa}$ when either θ_p is small or when $\kappa_p \approx \kappa_m$.

The energy difference between a protein on the tube versus on a flat membrane:

$$\Delta E = E^{\mathrm{b}}(tube) - E^{\mathrm{b}}(flat) = \frac{1}{2}\tilde{\kappa}A_P\left(\frac{1}{R_t} - C_0\right)^2 - \frac{1}{2}\tilde{\kappa}A_P(C_0)^2 = \frac{1}{2}\tilde{\kappa}A_P\left(\frac{1}{{R_t}^2} - \frac{2C_0}{R_t}\right) \quad (\mathrm{eq.\,S12})$$

ΔE describes the energy change of moving a protein-membrane complex from the flat membrane to the tube, where the tube-flat membrane geometry was pre-equilibrated (e.g., a tube pulled from a piece of flat membrane and is held by an external force). Note that the model predicts an energy cost of moving a 'flat protein' (C_0 =0), this is because the 'flat protein' will deform the pre-equilibrated tube, with an energy cost that is larger for bigger proteins. Therefore, the sorting of 'flat protein' is predicted to be smaller than 1. The reference molecule GPI has a negligible area in the membrane, ~1 nm^2, compared to Piezo1, therefore ΔE for GPI is negligible.

Assume the proteins on membrane can be approximated as 2D ideal gas (i.e., no interaction between proteins, density of protein on the membrane is low). The density of the protein on the tube relative to its density on the flat membrane follows the Boltzmann distribution:

$$S = \exp\left(\frac{-\Delta E}{k_B T}\right) = \exp\left[-\frac{\tilde{\kappa}A_P}{2k_B T}\left(\frac{1}{{R_t}^2} - \frac{2C_0}{R_t}\right)\right] \quad (\mathrm{eq.\,S13})$$

Note that eq. S13 is essentially the same as equation 8 of ref [30] or equation 2 of ref [34] (under low protein density and negligible protein-protein interaction), where free energy-based derivations were presented. Fitting eq. S13 to data in Fig. 2G, $\tilde{\kappa}A_P$ = 5000 $k_BT\cdot nm^2$ and $-C_0^{-1}$ = 87 nm, corresponding to the nano-geometry of Piezo1 under resting state. Fix $\tilde{\kappa}A_P$ = 5000

$k_BT \cdot nm^2$ and fit the data in Fig. 3D (+Yoda1) to eq. S13, we get C_0 = 0 nm^{-1}, corresponding to the nano-geometry of Piezo1 under open or inactive state.

Note that R_t is positive on protrusions, therefore, S is a monotonic increasing function of R_t. When R_t is negative (invaginations), S peaks at $R_t = C_0^{-1}$ (Fig. S8). Fig. S8 also shows that the effect of channel opening on Piezo1 sorting (changing C_0 from -87^{-1} nm^{-1} to 0 nm^{-1}) would almost diminish if the Piezo1 were 10 times smaller. Lastly, the curvature sensing on invaginations (negative R_t) would be significant if the 10-time smaller protein has a 10-time larger spontaneous curvature C_0 (8.7^{-1} nm^{-1}), similar to those of typical BAR domain proteins [34,40].

Acknowledgements

We thank Markus Deserno, Padmini Rangamani, Medha Pathak, Bianxiao Cui, Elizabeth Kelley, Navid Bavi, Andy Nieuwkoop and Deirdre O'Carroll for helpful discussions. We thank Bailong Xiao for providing quantifications of CryoEM images of Piezo1 containing liposomes. We thank Gill Fitz and Matt Tyska for helpful suggestions on filopodia quantification. We thank Renping Zhou and Zhiping Pang labs for helping with cell culture.

Author contributions

Z.S. and C.D.C. conceived the project. S.Y. carried out the experiments and analyzed the data. S.A. carried out measurements in Fig. S10 and in parts of Fig. 3. B.L. carried out measurements in Fig. S3 and in parts of Fig. 4. H.W. contributed to the preparations of HEK293T cells and plasmids. M.W. helped with Fig. S1D and theoretical modeling. Z.S. oversaw the experiments and data analysis of the entire project. Z.S., S.Y., and C.D.C. wrote the manuscript with input from all authors.

Declaration of Interests

The authors declare no competing interests.

References

1. Coste, B.; Mathur, J.; Schmidt, M.; Earley, T. J.; Ranade, S.; Petrus, M. J.; Dubin, A. E.; Patapoutian, A. Piezo1 and Piezo2 are essential components of distinct mechanically activated cation channels. *Science* **2010***, 330*, 55-60.

2. Coste, B.; Xiao, B.; Santos, J. S.; Syeda, R.; Grandl, J.; Spencer, K. S.; Kim, S. E.; Schmidt, M.; Mathur, J.; Dubin, A. E. Piezo proteins are pore-forming subunits of mechanically activated channels. *Nature* **2012***, 483*, 176-181.

3. Kefauver, J. M.; Ward, A. B.; Patapoutian, A. Discoveries in structure and physiology of mechanically activated ion channels. *Nature* **2020***, 587*, 567-576.

4. Murthy, S. E.; Dubin, A. E.; Patapoutian, A. Piezos thrive under pressure: mechanically activated ion channels in health and disease. *Nature Reviews Molecular Cell Biology* **2017***, 18*, 771-783.

5. Handler, A.; Ginty, D. D. The mechanosensory neurons of touch and their mechanisms of activation. *Nature Reviews Neuroscience* **2021***, 22*, 521-537.

6. Ge, J.; Li, W.; Zhao, Q.; Li, N.; Chen, M.; Zhi, P.; Li, R.; Gao, N.; Xiao, B.; Yang, M. Architecture of the mammalian mechanosensitive Piezo1 channel. *Nature* **2015***, 527*, 64-69.

7. Guo, Y. R.; MacKinnon, R. Structure-based membrane dome mechanism for Piezo mechanosensitivity. *Elife* **2017***, 6*, e33660.

8. Saotome, K.; Murthy, S. E.; Kefauver, J. M.; Whitwam, T.; Patapoutian, A.; Ward, A. B. Structure of the mechanically activated ion channel Piezo1. *Nature* **2018***, 554*, 481-486.

9. Zhao, Q.; Zhou, H.; Chi, S.; Wang, Y.; Wang, J.; Geng, J.; Wu, K.; Liu, W.; Zhang, T.; Dong, M.; Wang, J.; Li, X.; Xiao, B. Structure and mechanogating mechanism of the Piezo1 channel. *Nature* **2018***, 554*, 487-492.

10. Yang, X.; Lin, C.; Chen, X.; Li, S.; Li, X.; Xiao, B. Structure deformation and curvature sensing of PIEZO1 in lipid membranes. *Nature* **2022**, 1-7.

11. Cox, C. D.; Bae, C.; Ziegler, L.; Hartley, S.; Nikolova-Krstevski, V.; Rohde, P. R.; Ng, C.; Sachs, F.; Gottlieb, P. A.; Martinac, B. Removal of the mechanoprotective influence of the cytoskeleton reveals PIEZO1 is gated by bilayer tension. *Nature communications* **2016***, 7*, 1-13.

12. Lewis, A. H.; Grandl, J. Mechanical sensitivity of Piezo1 ion channels can be tuned by cellular membrane tension. *Elife* **2015***, 4*, e12088.

13. Haselwandter, C. A.; MacKinnon, R. Piezo's membrane footprint and its contribution to mechanosensitivity. *Elife* **2018***, 7*, e41968.

14. Bavi, N.; Richardson, J.; Heu, C.; Martinac, B.; Poole, K. PIEZO1-mediated currents are modulated by substrate mechanics. *ACS nano* **2019***, 13*, 13545-13559.

15. Wang, J.; Jiang, J.; Yang, X.; Zhou, G.; Wang, L.; Xiao, B. Tethering Piezo channels to the actin cytoskeleton for mechanogating via the cadherin-β-catenin mechanotransduction complex. *Cell Reports* **2022***, 38*, 110342.

16. Verkest, C.; Schaefer, I.; Nees, T. A.; Wang, N.; Jegelka, J. M.; Taberner, F. J.; Lechner, S. G. Intrinsically disordered intracellular domains control key features of the mechanically-gated ion channel PIEZO2. *Nature Communications* **2022***, 13*, 1-14.

17. Romero, L. O.; Caires, R.; Nickolls, A. R.; Chesler, A. T.; Cordero-Morales, J. F.; Vásquez, V. A dietary fatty acid counteracts neuronal mechanical sensitization. *Nature communications* **2020***, 11*, 1-12.

18. Shi, Z.; Graber, Z. T.; Baumgart, T.; Stone, H. A.; Cohen, A. E. Cell membranes resist flow. *Cell* **2018***, 175*, 1769-1779. e13.

19. Cohen, A. E.; Shi, Z. Do Cell Membranes Flow Like Honey or Jiggle Like Jello? *Bioessays* **2020***, 42*, 1900142.

20. Yao, M.; Tijore, A. S.; Cox, C. D.; Hariharan, A.; Van Nhieu, G. T.; Martinac, B.; Sheetz, M. Force-dependent Piezo1 recruitment to focal adhesions regulates adhesion maturation and turnover specifically in non-transformed cells. *bioRxiv* **2020**.

21. Ellefsen, K. L.; Holt, J. R.; Chang, A. C.; Nourse, J. L.; Arulmoli, J.; Mekhdjian, A. H.; Abuwarda, H.; Tombola, F.; Flanagan, L. A.; Dunn, A. R.; Parker, I.; Pathak, M. M. Myosin-II mediated traction forces evoke localized Piezo1-dependent Ca 2 flickers. *Communications biology* **2019***, 2*, 1-13.

22. Dumitru, A. C.; Stommen, A.; Koehler, M.; Cloos, A.; Yang, J.; Leclercqz, A.; Tyteca, D.; Alsteens, D. Probing PIEZO1 Localization upon Activation Using High-Resolution Atomic Force and Confocal Microscopy. *Nano Letters* **2021***, 21*, 4950-4958.

23. Lin, Y.; Guo, Y. R.; Miyagi, A.; Levring, J.; MacKinnon, R.; Scheuring, S. Force-induced conformational changes in PIEZO1. *Nature* **2019***, 573*, 230-234.

24. Holt, J. R.; Zeng, W.; Evans, E. L.; Woo, S.; Ma, S.; Abuwarda, H.; Loud, M.; Patapoutian, A.; Pathak, M. M. Spatiotemporal dynamics of PIEZO1 localization controls keratinocyte migration during wound healing. *Elife* **2021***, 10*, e65415.

25. Chen, X.; Wanggou, S.; Bodalia, A.; Zhu, M.; Dong, W.; Fan, J. J.; Yin, W. C.; Min, H.; Hu, M.; Draghici, D. A feedforward mechanism mediated by mechanosensitive ion channel PIEZO1 and tissue mechanics promotes glioma aggression. *Neuron* **2018***, 100*, 799-815. e7.

26. Jiang, F.; Yin, K.; Wu, K.; Zhang, M.; Wang, S.; Cheng, H.; Zhou, Z.; Xiao, B. The mechanosensitive Piezo1 channel mediates heart mechano-chemo transduction. *Nature communications* **2021***, 12*, 1-14.

27. Carrillo-Garcia, J.; Herrera-Fernández, V.; Serra, S. A.; Rubio-Moscardo, F.; Vogel-Gonzalez, M.; Doñate-Macian, P.; Hevia, C. F.; Pujades, C.; Valverde, M. A. The mechanosensitive Piezo1 channel controls endosome trafficking for an efficient cytokinetic abscission. *Science advances* **2021***, 7*, eabi7785.

28. Efremov, A. K.; Yao, M.; Sun, Y.; Tee, Y. H.; Sheetz, M. P.; Bershadsky, A. D.; Martinac, B.; Yan, J. Application of piconewton forces to individual filopodia reveals mechanosensory role of L-type Ca2 channels. *Biomaterials* **2022**, 121477.

29. Syeda, R.; Xu, J.; Dubin, A. E.; Coste, B.; Mathur, J.; Huynh, T.; Matzen, J.; Lao, J.; Tully, D. C.; Engels, I. H. Chemical activation of the mechanotransduction channel Piezo1. *Elife* **2015***, 4*, e07369.

30. Rosholm, K. R.; Leijnse, N.; Mantsiou, A.; Tkach, V.; Pedersen, S. L.; Wirth, V. F.; Oddershede, L. B.; Jensen, K. J.; Martinez, K. L.; Hatzakis, N. S.; Bendix, P. M.; Callen-Jones Andrew; Stamou, D. Membrane curvature regulates ligand-specific membrane sorting of GPCRs in living cells. *Nature chemical biology* **2017***, 13*, 724-729.

31. Lauritzen, I.; Chemin, J.; Honoré, E.; Jodar, M.; Guy, N.; Lazdunski, M.; Jane Patel, A. Cross-talk between the mechano-gated K2P channel TREK-1 and the actin cytoskeleton. *EMBO Rep.* **2005***, 6*, 642-648.

32. Mattila, P. K.; Lappalainen, P. Filopodia: molecular architecture and cellular functions. *Nature reviews Molecular cell biology* **2008***, 9*, 446-454.

33. Charras, G. T.; Yarrow, J. C.; Horton, M. A.; Mahadevan, L.; Mitchison, T. J. Non-equilibration of hydrostatic pressure in blebbing cells. *Nature* **2005***, 435*, 365-369.

34. Prévost, C.; Zhao, H.; Manzi, J.; Lemichez, E.; Lappalainen, P.; Callan-Jones, A.; Bassereau, P. IRSp53 senses negative membrane curvature and phase separates along membrane tubules. *Nature communications* **2015***, 6*, 1-11.

35. Lewis, A. H.; Grandl, J. Piezo1 ion channels inherently function as independent mechanotransducers. *Elife* **2021***, 10*, e70988.

36. Jiang, W.; Del Rosario, J. S.; Botello-Smith, W.; Zhao, S.; Lin, Y.; Zhang, H.; Lacroix, J.; Rohacs, T.; Luo, Y. L. Crowding-induced opening of the mechanosensitive Piezo1 channel in silico. *Communications Biology* **2021***, 4*, 1-14.

37. Ridone, P.; Pandzic, E.; Vassalli, M.; Cox, C. D.; Macmillan, A.; Gottlieb, P. A.; Martinac, B. Disruption of membrane cholesterol organization impairs the activity of PIEZO1 channel clusters. *J. Gen. Physiol.* **2020***, 152*.

38. Lou, H.; Zhao, W.; Li, X.; Duan, L.; Powers, A.; Akamatsu, M.; Santoro, F.; McGuire, A. F.; Cui, Y.; Drubin, D. G. Membrane curvature underlies actin reorganization in response to nanoscale surface topography. *Proceedings of the National Academy of Sciences* **2019***, 116*, 23143-23151.

39. De Vecchis, D.; Beech, D. J.; Kalli, A. C. Molecular dynamics simulations of Piezo1 channel opening by increases in membrane tension. *Biophys. J.* **2021**.

40. Shi, Z.; Baumgart, T. Membrane tension and peripheral protein density mediate membrane shape transitions. *Nature communications* **2015***, 6*, 1-8.

41. Song, Y.; Li, D.; Farrelly, O.; Miles, L.; Li, F.; Kim, S. E.; Lo, T. Y.; Wang, F.; Li, T.; Thompson-Peer, K. L. The mechanosensitive ion channel piezo inhibits axon regeneration. *Neuron* **2019***, 102*, 373-389. e6.

42. Ma, N.; Chen, D.; Lee, J.; Kuri, P.; Hernandez, E. B.; Kocan, J.; Mahmood, H.; Tichy, E. D.; Rompolas, P.; Mourkioti, F. Piezo1 regulates the regenerative capacity of skeletal muscles via orchestration of stem cell morphological states. *Science advances* **2022***, 8*, eabn0485.

43. Nilufar, S.; Morrow, A. A.; Lee, J. M.; Perkins, T. J. FiloDetect: automatic detection of filopodia from fluorescence microscopy images. *BMC systems biology* **2013***, 7*, 1-12.

44. Wang, H.; Kelley, F. M.; Milovanovic, D.; Schuster, B. S.; Shi, Z. Surface tension and viscosity of protein condensates quantified by micropipette aspiration. *Biophysical Reports* **2021**, 100011.

45. Stachowiak, J. C.; Schmid, E. M.; Ryan, C. J.; Ann, H. S.; Sasaki, D. Y.; Sherman, M. B.; Geissler, P. L.; Fletcher, D. A.; Hayden, C. C. Membrane bending by protein–protein crowding. *Nat. Cell Biol.* **2012***, 14*, 944-949.

46. Derényi, I.; Jülicher, F.; Prost, J. Formation and interaction of membrane tubes. *Phys. Rev. Lett.* **2002***, 88*, 238101.

47. Kang, M.; Day, C. A.; Kenworthy, A. K.; DiBenedetto, E. Simplified equation to extract diffusion coefficients from confocal FRAP data. *Traffic* **2012***, 13*, 1589-1600.

Materials

Chemicals

Name	Source	Catalog Number
EMEM	Fisher scientific	MT10009CV(Corning™)
DMEM	Fisher scientific	11965092
FBS	Fisher scientific	FB12999102(Fisherbrand™)
Sodium Pyruvate	Fisher scientific	11360070
Penicillin-Streptomycin	ThermoFisher scientific	15070063(Gibco™)
PBS	ThermoFisher scientific	10010023(Gibco™)
Trypsin	ThermoFisher scientific	25300054(Gibco™)
Opti-MEM	ThermoFisher scientific	31985070(Gibco™)
TransIT-X2	Mirus	MIR6003(Mirus)
Lipofectamine 3000	ThermoFisher scientific	L3000001
NaCl	Fisher scientific	BP358-212(Fisher BioReagents)
KCl	Millipore Sigma	7300-500GM(Millipore)
HEPES	Fisher scientific	BP310-1(Fisher BioReagents)
Glucose	Fisher scientific	BP350-1(Fisher BioReagents)
$CaCl_2$	Fisher scientific	C79-500
$MgCl_2$	Fisher scientific	M33-500
Yoda1	Millipore Sigma	SML1558-5MG(Sigma-Aldrich)
Latrunculin B	AdipoGen	AG-CN2-0031-M001(AdipoGen)
4.5 µm bead	Spherotech	DIGP-40-2
Matrigel	Fisher scientific	354234
PDL	Millipore Sigma	P7405-5MG(Sigma-Aldrich)
DMSO	Fisher scientific	BP231-100

Plasmids

Name	Source	Catalog #
eGFP-CaaX	Adam Cohen lab	N.A.
GPI-eGFP	Addgene	32601
GPI-mCherry	Addgene	127812
hPiezo1-eGFP	Charles Cox lab, eGFP fused at position 1591 of human Piezo1	N.A.
hPiezo1-mCherry	Charles Cox lab, mCherry fused at position 1591 of human Piezo1	N.A.
mOrange2-CaaX	Adam Cohen lab	N.A.
mPiezo1-mCherry	Ardem Patapoutian lab, mCherry fused at the C-terminus of mouse Piezo1	N.A.
mTREK1-mCherry	Philip Gottlieb lab	N.A.
SNAP-D2R-eGFP	Adam Cohen lab	N.A.

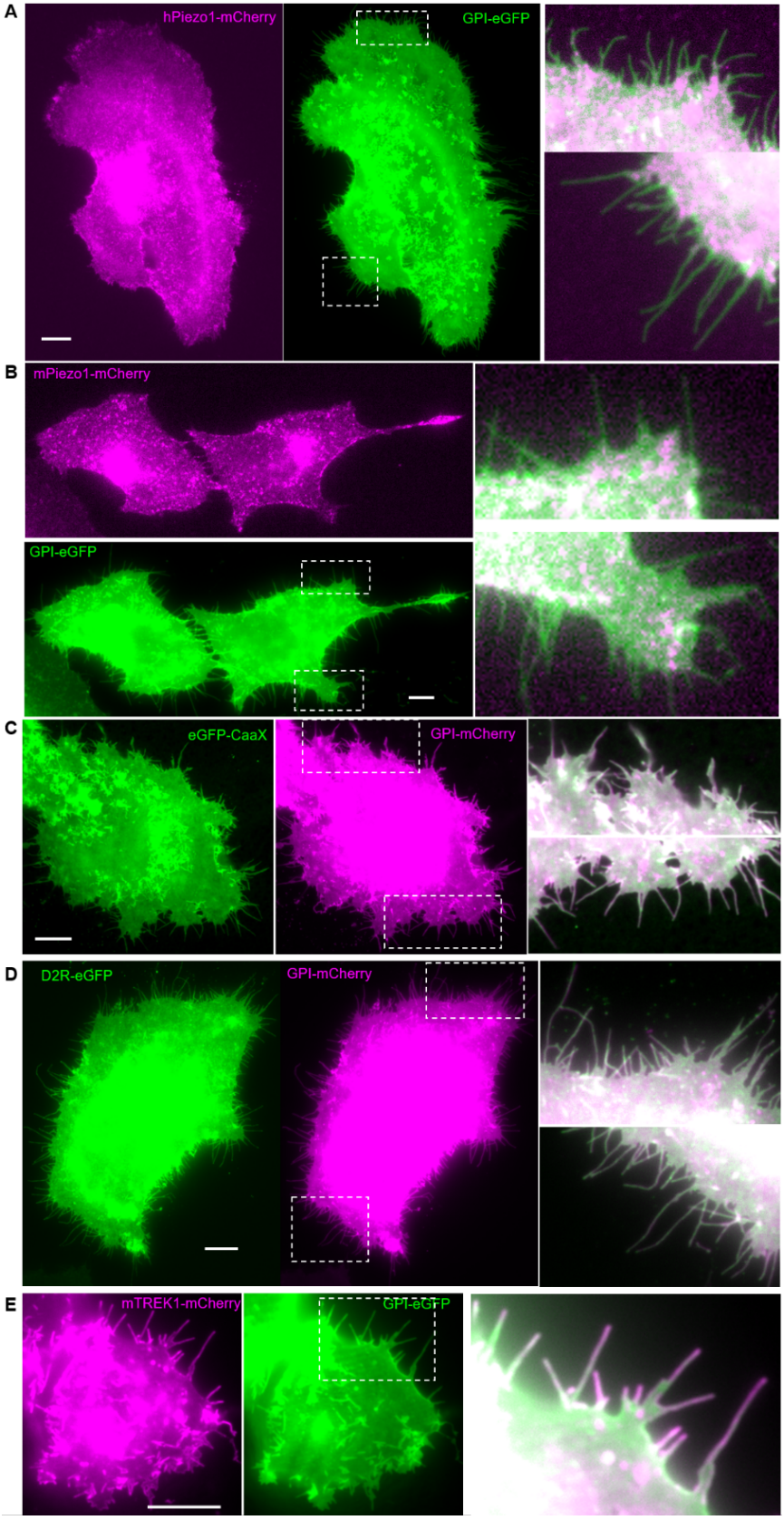

Figure S1. Fluorescence images corresponding to Fig. 1D

Figure S1. Fluorescence images of HeLa cells co-expressing: **(A)** hPiezo1-mCherry (magenta) and GPI-eGFP (green); **(B)** mPiezo1-mCherry (magenta) and GPI-eGFP (green); **(C)** eGFP-CaaX (green) and GPI-mCherry (magenta); **(D)** D2R-eGFP (green) and GPI-mCherry (magenta). **(E)** Fluorescence images of HEK-293T cells co-expressing mTREK1-mCherry (magenta) and GPI-eGFP (green). The boxed regions are merged and contrast-adjusted on the right. All scale bars are 10 µm.

Figure S2. Calculation of membrane curvature sorting and filopodia/tether radii

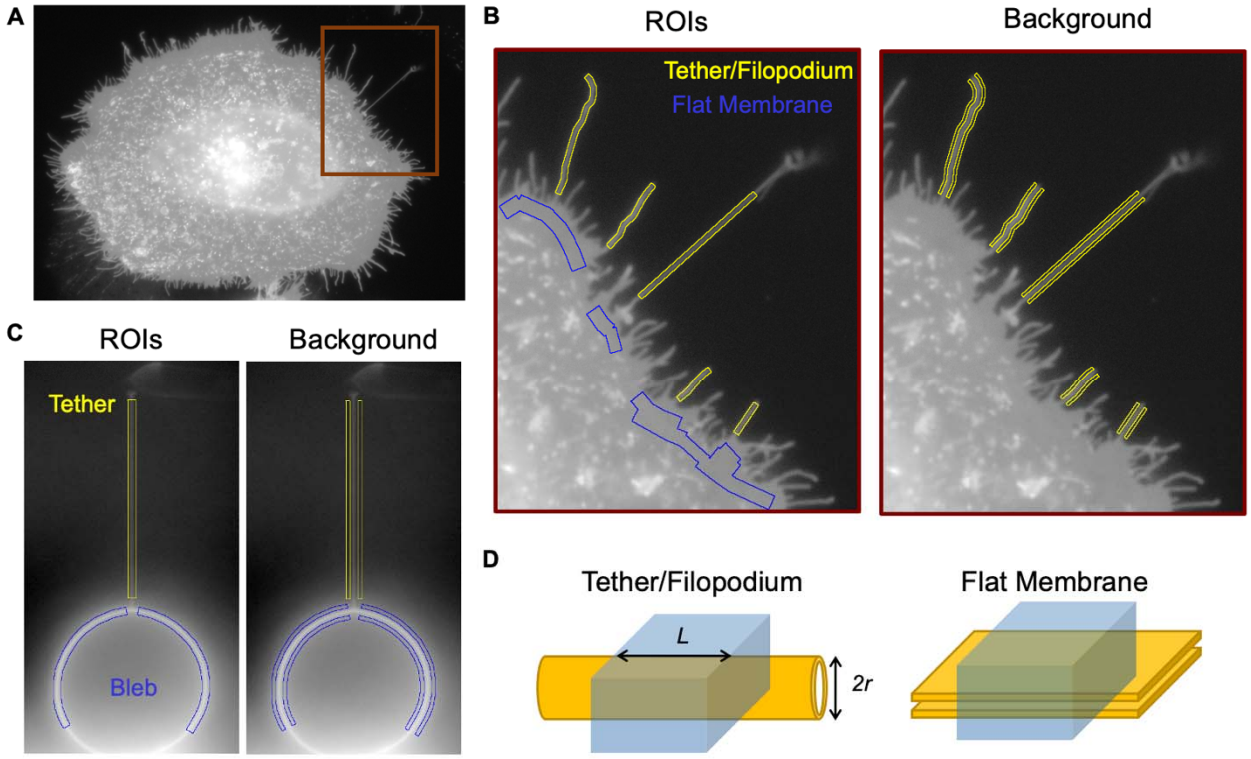

Figure S2. (A) Fluorescence images of a HeLa cell in the GPI-mCherry channel (intensity in log scale), with the boxed region enlarged in (**B**). **(B)** Left: ROIs for each tether/filopodium boxed in yellow, flat regions on the cell body boxed in blue. Right: two background regions for each ROI boxed in yellow. **(C)** Left: ROIs for a tether (yellow) and for a bleb (blue). Right: two background regions corresponding to each ROI on the left. **(D)** Illustration to show the imaged regions of a cylindrical tether/filopodium (left) and a flat cell membrane (right). Illumination profile shown in blue.

Figure S3. Depletion of Piezo1 from filopodia of HEK293T cells

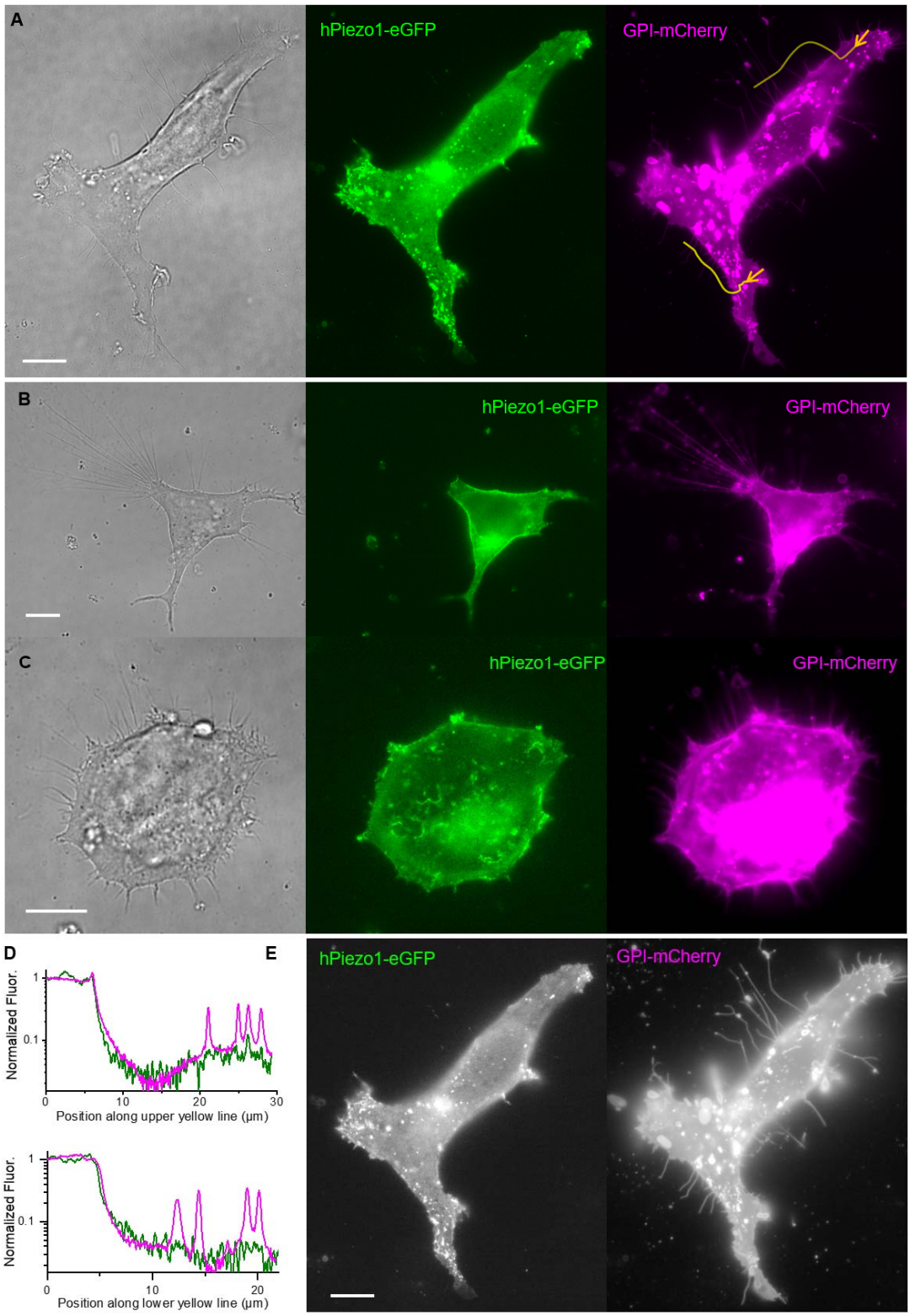

Figure S3. (A-C): Transmitted light (left), hPeizo1-eGFP fluorescence (middle), and GPI-mCherry (right) images of HEK293 cells. **(D)** Fluorescent intensity along the two yellow lines shown in (**A**). **(E)** log-fluorescence of (**A**). All scale bars are 10 μm.

Figure S4. Curvature sensitivity of Pieoz1 and D2R on filopodia

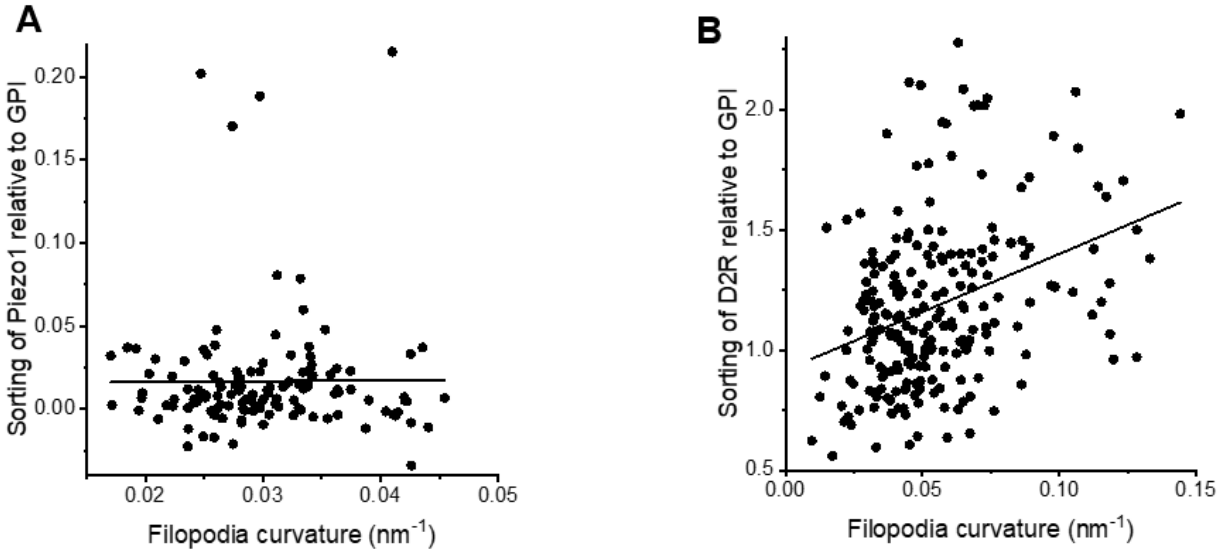

Figure S4. (A) Sorting of hPiezo1 does not change with filopodia curvature (black line: linear fit with slope 0.05 ± 0.51 nm), Person's r value = 0.009. **(B)** Sorting of DRD2 increases with filopodia curvature (black line: linear fit with slope 4.83 ± 0.86 nm), Person's r value = 0.35.

Figure S5. Sorting of Piezo1 does not change with the relaxation of tether radius.

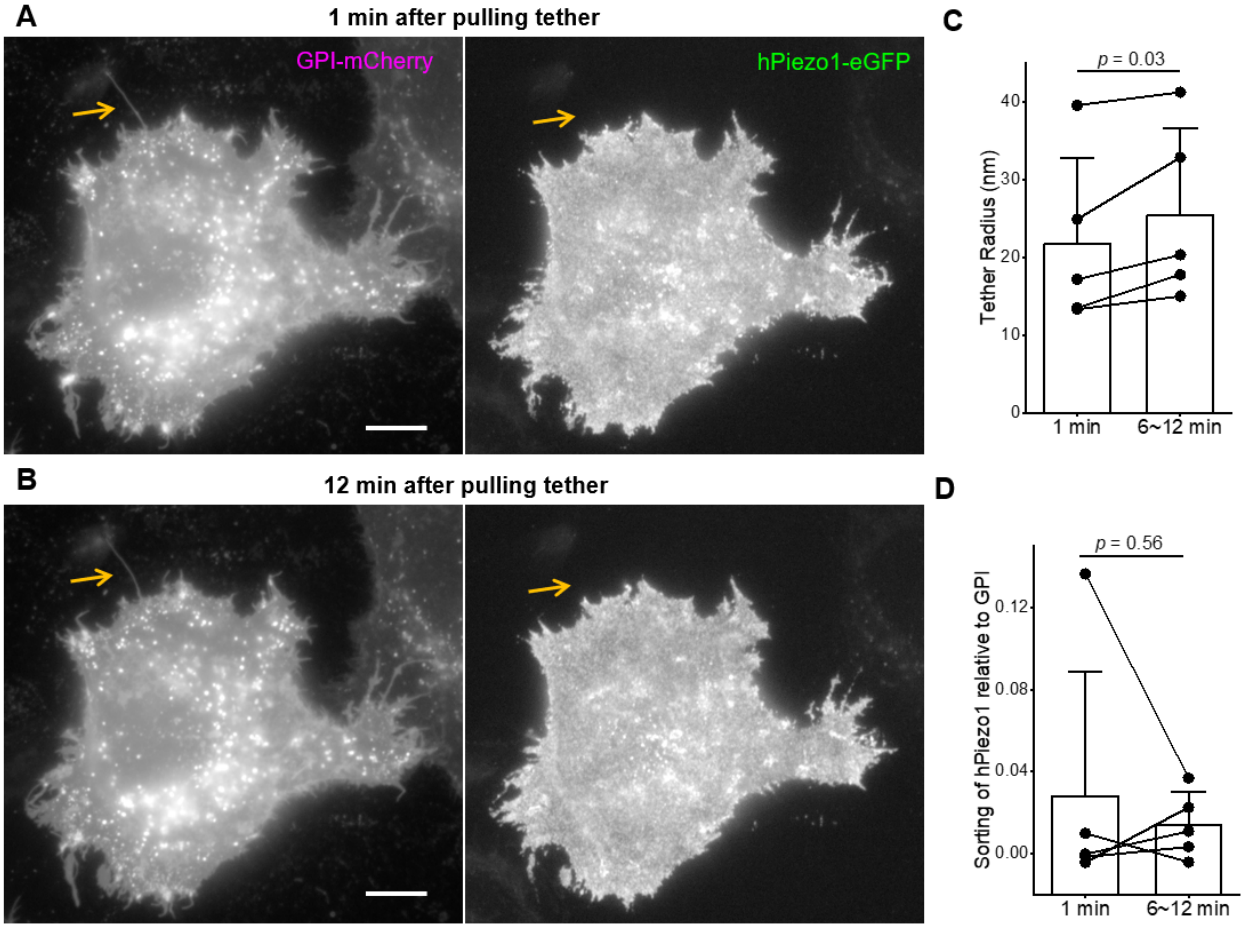

Fluorescence images of a HeLa cell co-expressing GPI-mCherry (left) and hPiezo1-eGFP (right), 1 min after pulling tether (**A**) and 12 min after pulling tether (**B**). Arrows point to the tether. The sorting of hPiezo1 was (0.010 ± 0.010) 1 min after tether pulling and was (-0.004 ± 0.011) 12 min after tether pulling, while the tether radius changed from (17.19 ± 0.05) nm to (20.33 ± 0.06) nm. Representative of 5 tethers and cells. All fluorescence images here are shown in log-scale to highlight the dim tether. All scale bars are 10 µm. Change of tether radius (**C**) and Piezo1 sorting on tethers (**D**) (1min vs. 6~12 min after tether pulling). Bar plot shows mean + S.D., *p* values given by paired Student's t test.

Figure S6: Upper limit of the tether radii from blebs

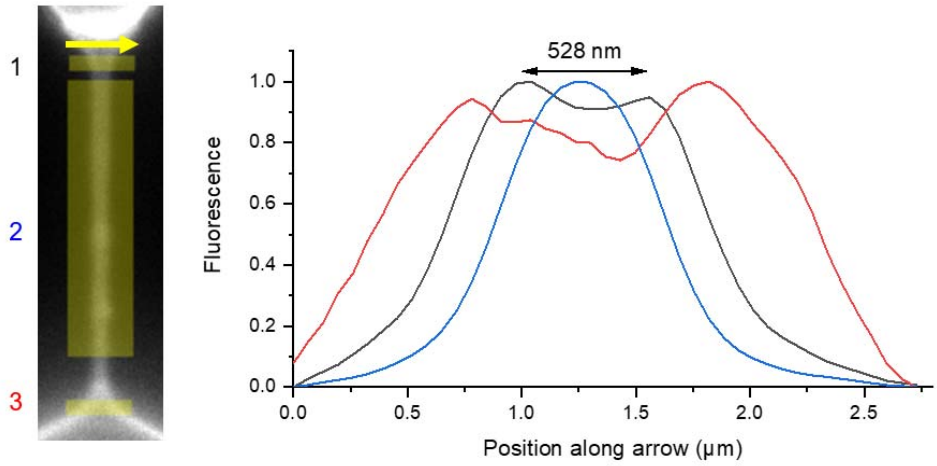

Left: fluorescence image of the thickest tether pulled from a bleb (Fig. 2D). The shape of the tether gradually changes from cylindrical to catenoid-shape at the connections of the tether to the pulling handle and to the bleb, consistent with the behavior of low-tension membrane tubes [46]. The measured apparent radius of the tether was (0.671 ± 0.003) A.U., which converts to an absolute diameter of 485 ± 82 nm. The conversion factor (361 ± 61 nm/A.U.) was determined by assuming that the average radius of filopodia and equilibrated tethers from cell body equal to the radii of tethers from tense blebs (Fig. 2G). Three yellow lines marked on the image: 1, a line across the tether-pipette junction; 2, a line across the majority of the tether (used for determining the apparent radius the tether); 3, a line across the tether-bleb junction.

Right: normalized fluorescence intensity profiles along the three lines marked on the left. The majority of the tether radius was within optical resolution (blue), while a peak-to-peak distance of 528 nm was measured from the fluorescence across the tether-pipette junction (black), serving as an upper limit of the absolute diameter for this tether. A peak-to-peak distance of 1047 nm was measured from the fluorescence across the tether-bleb junction (red).

Figure S7. Measurements of cell membrane bending stiffness

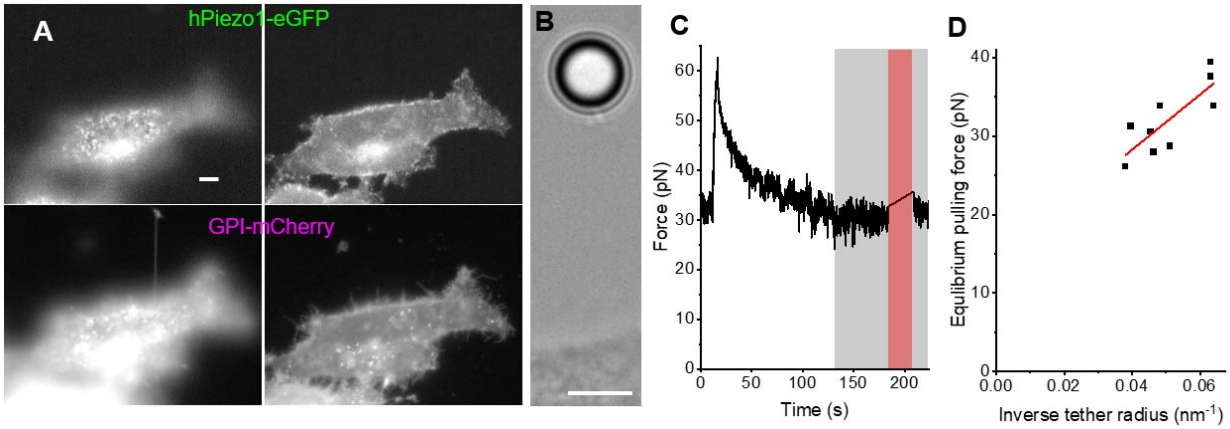

(A) A HeLa cell expressing hPiezo1-eGFP (up) and GPI-mCherry (down), with a 15 μm tether pulled by an optically trapped 4.5 μm diameter bead. Left: focus on the tether. Right: focus on the cell body. **(B)** Transmitted light image of the optically trapped bead that was used for calculating tether pulling force. All scale bars are 5 μm. **(C)** Time dependent tether pulling force after stretching the tether at t = 10 s. Images in (**A**) were taken during the period shaded in red, from which a 26.3 nm tether radius (based on GPI fluorescence) was determined. The gray area was used to calculate the equilibrated pulling force (30.5 pN). **(D)** Experiments of equilibrium tether pulling force vs. inverse tether radius repeated on 9 tethers pulled from 6 independent cells. The red line is a linear fit, with a positive intercept (14 ± 5 pN) potentially corresponding to contributions of cytoskeleton attachments and membrane asymmetry. The slope of the fit (351 ± 99 pN·nm) gave the cell membrane bending stiffness 13.6 ± 3.8 k_BT.

Figure S8. Modeling the curvature sorting of Piezo1

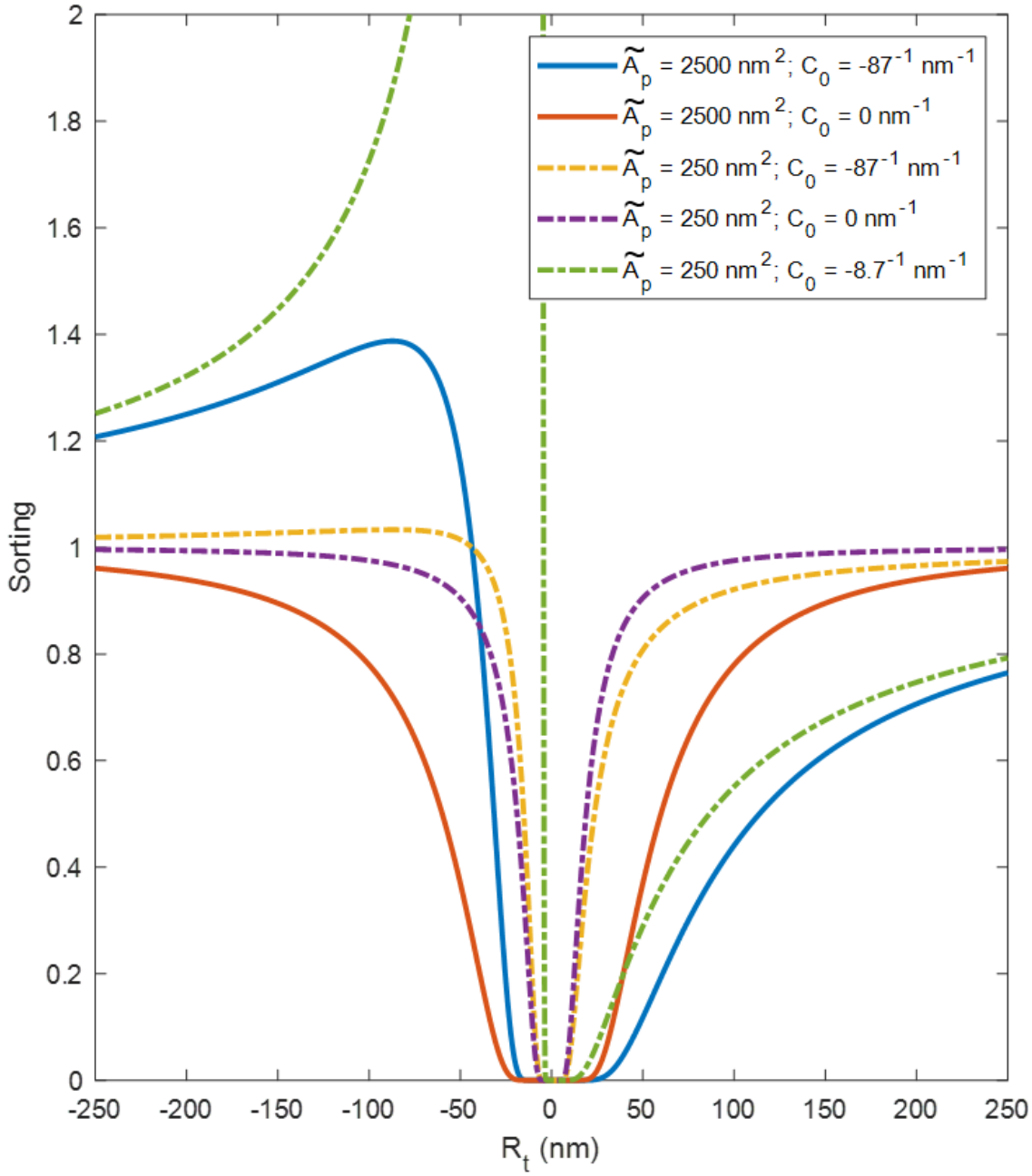

Sorting of Piezo1 as a function of tube radius (eq. 1) plotted using parameters that correspond to closed Piezo1 (blue, based on data in Fig. 2G) and open/inactivated Piezo1 (orange, based on data in Fig. 3D). Negative R_t corresponds to membrane invaginations. The curvature sorting of a hypothetical ion channel with 1/10 of the area of Piezo1 are plotted in yellow (closed) and purple (open/inactive), showing that the opening of the channel has less significant effect on its curvature sorting if the area is small. The sorting of a hypothetical protein with 1/10 of the area of Piezo1 and 10 times higher spontaneous curvature is plotted in green, showing strong curvature sensitivity to invaginations, similar to that of N-BAR domain containing proteins.

Figure S9. Full images for Fig. 3A, 3F

A

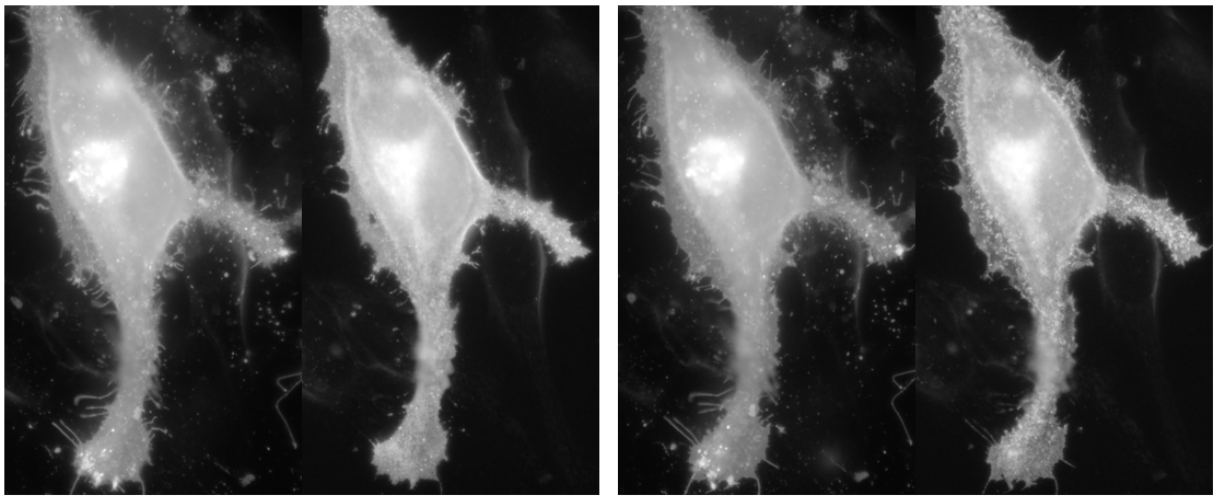

B

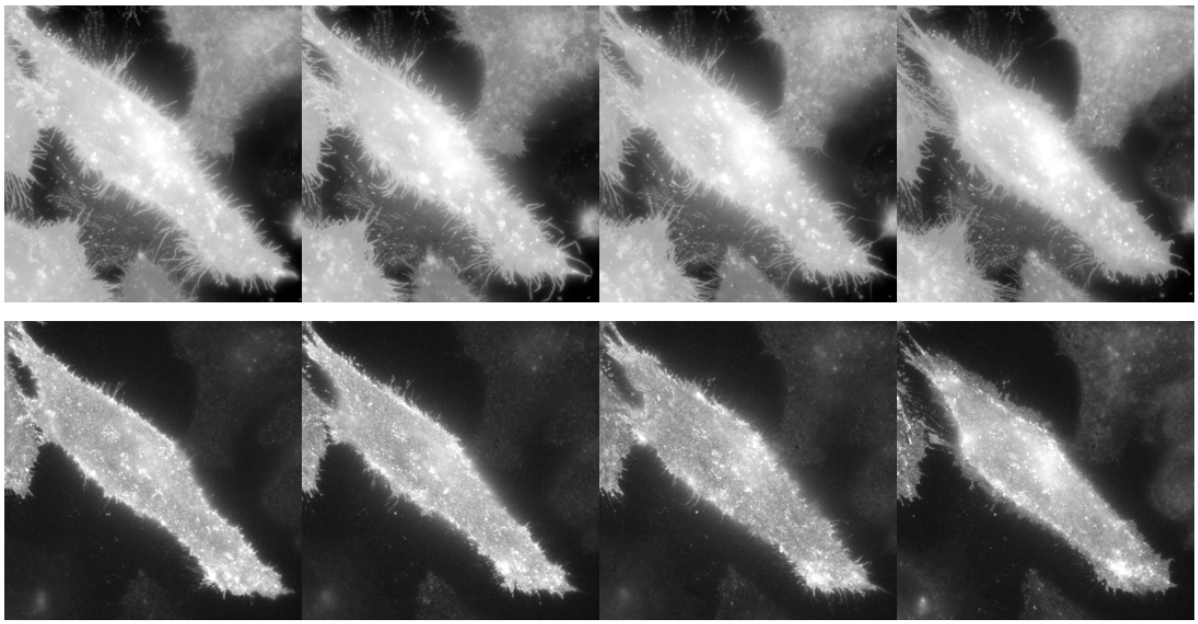

(A) Full image of Fig. 3A. **(B)** Full image of Fig. 3F

Figure S10. Kinetics of hPiezo1 on plasma membranes

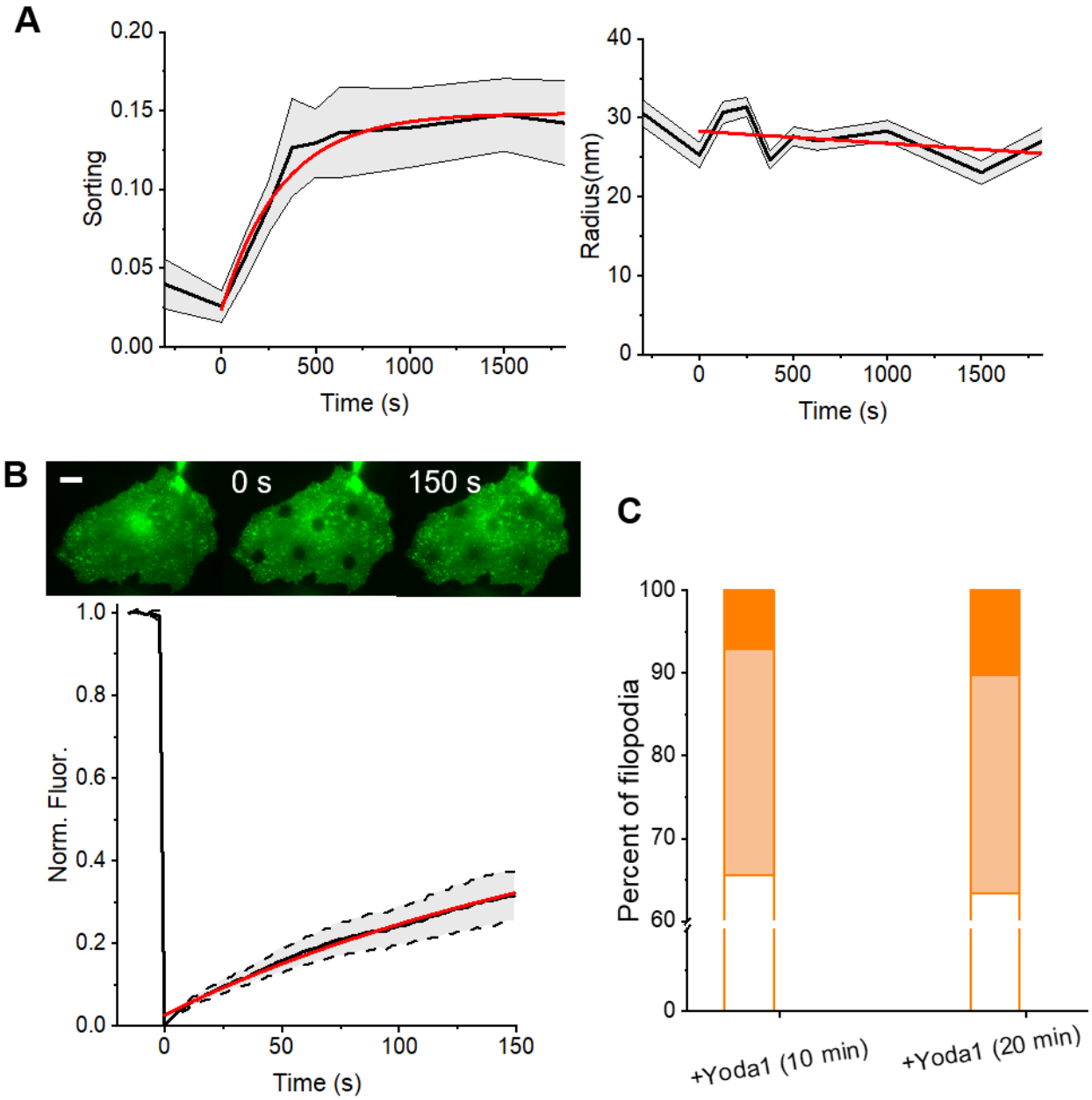

(**A**) Change of Piezo1 sorting on filopodia (left) and filopodia radii (right) after adding 100 µM Yoda1. (**B**) Fluorescence recovery after photobleaching (FRAP) of hPiezo1-eGFP in HeLa cells. Red line: fitting to eq. S8, $\tau_{0.5}$ = 342 ± 4 s, r^2 = 0.994. Error bars are standard deviation. Scale bar, 5 µm. (**C**) Percentage of filopodia that showed strong (S_{filo} > 0.3, dark), medium (0.1 < S_{filo} < 0.3, light), and weak (S_{filo} < 0.1, open) sorting of hPiezo1 10 min and 20 min after adding Yoda1. 10 µM Yoda1 was added after hypotonic shock.